

Local Analogs to High-Redshift Galaxies: I. Characterization of Dust Emission and Star Formation History

SKARLETH M. MOTIÑO FLORES,¹ TOMMY WIKLIND,² AND RAFAEL T. EUFRASIO³

¹*Physics Department, The Catholic University of America, 620 Michigan Ave. NE, Washington, DC 20064, USA*

²*Physics Department, The Catholic University of America, 620 Michigan Ave. NE, Washington, DC 20064*

³*Department of Physics, University of Arkansas, 248 Physics Building, 825 West Dickson Street, Fayetteville, AR 72701, USA*

Submitted to ApJ

Abstract

Star-forming dwarf galaxies have properties similar to those expected in high-redshift galaxies. Hence, these local galaxies may provide insights into the evolution of the first galaxies, and the physical processes at work. We present a sample of eleven potential local analogs to high- z (LAHz) galaxies. The sample consists of blue compact dwarf galaxies, selected to have spectral energy distributions that fit galaxies at $1.5 < z < 4$. We use SOFIA-HAWC+ observations combined with optical and near-infrared data to characterize the dust properties, star formation rate (SFR) and star formation histories (SFH) of the sample of LAHz. We employ Bayesian analysis to characterize the dust using two component black-body models. Using the LIGHTNING package we fit the spectral energy distribution of the LAHz galaxies over the FUV-FIR wavelength range, and derive the SFH in five time-steps up to a look-back time of 13.3 Gyr. Of the eleven LAHz candidates, six galaxies have SFH consistent with no star formation activity at look-back times beyond 1 Gyr. The remaining galaxies show residual levels of star formation at ages $\gtrsim 1$ Gyr, making them less suitable as local analogs. The six young galaxies stand out in our sample by having the lowest gas-phase metallicities. They are characterized by warmer dust, having the highest specific SFR, and the highest gas mass fractions. The young age of these six galaxies suggests that merging is less important as a driver of the star formation activity. The six LAHz candidates are promising candidates for studies of the gas dynamics role in driving star formation.

Keywords: galaxies: blue compact dwarf galaxies, local analogs, high-redshift - infrared: photometry - infrared: ISM, dust - SFH: Star Formation History - SFR: Star Formation Rate.

1. INTRODUCTION

The high-redshift (high- z) universe is very different from our local environment: galaxies are physically small with irregular morphologies; they are metal-poor, star formation rates (SFRs) are high and growing exponentially, and the interstellar gas constitutes a major component of the total baryonic mass. However, the faintness and the small sizes make it extremely difficult to study the physical processes in these galaxies in detail. Instead, a significant effort over the last decade has been devoted to identifying low-redshift (low- z) analogs to high- z galaxies. (e.g. [Bian et al. 2016](#), [Sebastian & Bait 2019](#)). These analogs to high- z galaxies, are usually local low metallicity, star forming dwarf galaxies. They share many properties of high-redshift galaxies in terms of morphology, physical size, metallicity and star formation (e.g. [Kaaret et al. 2011](#), [Adamo et al. 2011](#); [Östlin et al. 2014](#)). This provides an attractive route to study the properties of high- z galaxies in better detail.

Several previous studies have defined analogs to high- z galaxies using a variety of approaches. For instance, [Heckman et al. \(2005\)](#) and [Hoopes et al. \(2007\)](#) found that ultra-violet luminous galaxies (UVLGs) with high surface brightness

have characteristics that are remarkably similar to Lyman break galaxies (LBGs) at high- z . UVLGs are rare in the local universe, but a significant sample can be defined when extending the search to $z \sim 0.2$. These Lyman Break Analogs have $L_{UV} \gtrsim 2 \times 10^{10} L_{\odot}$, star formation rates (SFR) of $3\text{--}30 M_{\odot} \text{ yr}^{-1}$, sizes of a few kpc, and sub-Solar metallicities. In a similar manner, [Overzier et al. \(2011\)](#) defines analogs of high- z LBGs based on their UV luminosity. [Östlin et al. \(2014\)](#) uses $H\alpha$ equivalent widths as a requirement to identify local galaxies that have $\text{Ly}\alpha$ luminosities comparable to high redshift $\text{Ly}\alpha$ Emitters (LAEs) and LBGs (the $\text{Ly}\alpha$ Reference Sample, or LARS). The galaxies comprising LARS are small, metal-poor, $\sim 0.2\text{--}0.6 Z_{\odot}$, gas-rich, with an average gas mass fraction ~ 0.4 , and SFRs ranging from 0.6 to $\sim 20 M_{\odot} \text{ yr}^{-1}$. They are morphologically identified as dwarf irregular galaxies ([Pardy et al. \(2014\)](#)). Interestingly, most of the LAE and LBG analogs defined by [Östlin et al. \(2014\)](#) are also far-infrared bright, showing the presence of significant amounts of dust in their interstellar medium, including one galaxy with a $\text{Ly}\alpha$ escape fraction of $\sim 12\%$.

Another proposed analog for high redshift LAEs is the class of Green Peas ([Cardamone et al. 2009](#)). These are compact, low-mass galaxies, with sub-Solar metallicities. They have SFRs of $\sim 4 M_{\odot} \text{ yr}^{-1}$, but very high specific star formation rates ([Izotov et al. 2011](#)). Their properties overlap with Blue Compact Dwarf galaxies (BCDGs) at the high luminosity end of BCDGs, but are otherwise distinct. Green Peas exhibit starburst driven outflows ([Yang et al. 2017](#)) and many have a high $\text{Ly}\alpha$ escape fraction ([Kim et al. 2021](#)). The typical distance of Green Peas is $z \sim 0.2\text{--}0.3$.

Although these analogs to high- z galaxies are ‘local’ in a cosmological sense, they are still quite distant as far as detailed studies are concerned. The UVLGs and Green Peas are at $z \sim 0.2 - 0.3$, or $D_A \gtrsim 700$ Mpc, while the average distance to galaxies in the LARS sample is ~ 300 Mpc. In linear scale, this correspond to $\gtrsim 3.3$ and 1.5 kpc/arcsecond, respectively. The relatively large distances are necessary because of the low number densities of galaxies fulfilling the criteria for being selected as an LBG and/or LAE analog.

In this paper we present an alternative approach to define local analogs, that allows us to select nearby galaxies at distances $\sim 10\text{--}20$ Mpc. This means that scales of 50 pc can be resolved even with ground-based instruments. Instead of matching properties like luminosity and/or equivalent widths of emission lines, this approach relies on how well the entire UV to near-infrared spectral energy distribution (SED) of local galaxies match those of high- z galaxies. Using templates of local galaxies spanning a wide variety of morphology, star formation activity, gas-phase metallicity, as well as AGN activity and environment, we identify those templates that are most successful in fitting high redshift galaxies as potential local analogs to high- z galaxies (LAHz). The sample of LAHz presented in this work, is selected from 129 local galaxy spectral templates compiled by [Brown et al. \(2014\)](#). These templates are fit to $\sim 180,000$ high redshift galaxies in the CANDELS (Cosmic Assembly Near-infrared Deep Extragalactic Legacy Survey) fields. It turns out that only a small number of the local templates provide the best-fit SED to galaxies at $z > 2$. All the local templates in this category are designated as blue compact dwarf galaxies. The LAHz are thus scaled-down versions of star forming high redshift galaxies.

All of the LAHz, as well as most of the galaxies in the $\text{Ly}\alpha$ Reference Sample ([Östlin et al. 2014](#)) are detected at far-infrared (FIR) wavelengths, suggesting thermal dust emission. The connection between star formation activity and dust content in galaxies is well-established, and provides information about the evolutionary stage of galaxies. In a study involving ~ 1600 low-redshift galaxies, [da Cunha et al. \(2010\)](#) found a strong correlation between the dust-to-stellar mass ratio and the specific star formation rate, as well as a strong correlation between the dust-to-SFR ratio and sSFR. These correlations suggests an evolutionary sequence and can be used as diagnostic for inferring the evolutionary stage of galaxies in combination with other parameters, like the star formation history (SFH).

Observations with the Atacama Large Millimeter Array (ALMA) over the last few years have vastly increased our understanding of the cold and dense interstellar medium of galaxies in the early universe. Star-forming galaxies on the Main Sequence (MS) at $z \sim 3$ appear to have dust attenuation properties similar to large and massive star-forming galaxies in our local universe ([Fudamoto et al. 2017](#)). Recent results from the ALPINE survey ([Le Fèvre et al. 2020](#)), however, suggest that the dust attenuation decreases drastically for galaxies on the MS at $z \gtrsim 4$ ([Fudamoto et al. 2020](#)), approaching that of metal-poor dwarf galaxies in the local universe.

The shape of the far-infrared dust SED of high- z galaxies has largely remained unconstrained, as most rest-frame FIR observations at high- z consists of a single photometric data point. This is also changing thanks to data from ALMA. The FIR SED can now be constructed for galaxies at $z \sim 2$, where [Pantoni et al. \(2021\)](#) find luminosity-weighted dust temperatures ~ 50 K for 11 galaxies on the MS. [Faisst et al. \(2020\)](#) measured the dust SED for a handful a MS galaxies at $z \gtrsim 4$, showing that the peak temperatures characterizing the dust SEDs are warmer than for star-forming galaxies in the local universe.

In this paper we provide a detailed characterization of the dust in our sample of local analogs to high redshift (LAHz) galaxies. We present new SOFIA HAWC+ observations which, together with ancillary data, allow us to define the dust SED in detail. This is used to evaluate whether they share properties with galaxies at high redshift, or whether they are similar to local massive star-forming galaxies.

This paper is organized as follows: In Section. 2 we describe the sample definition and selection method. In Section. 3 we describe our SOFIA observations and ancillary data used. In Section. 4 we describe the two modeling procedures used to characterize the dust continuum and the FUV to FIR SED. In Section. 5 we present the dust properties and SFHs and in Section. 6 discuss the implications of this results. In Section. 7 we summarize our results and conclusions about the properties of our sample of LAHz.

2. SAMPLE DEFINITION

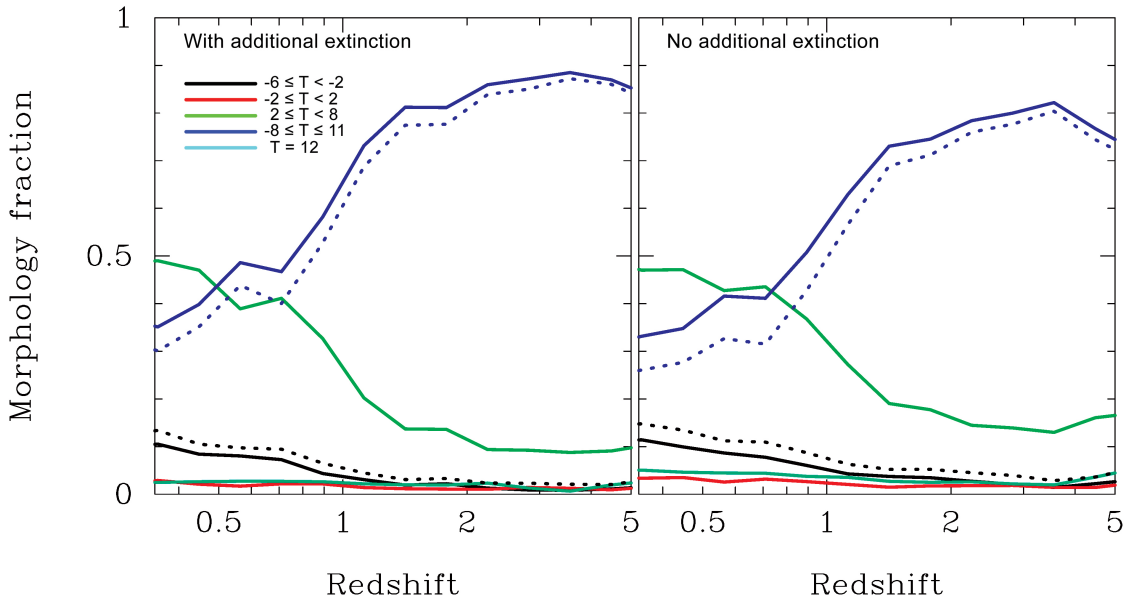


Figure 1. The morphology fraction of the Brown et al. (2014) templates, divided into four groups based on morphological T-class. The fraction for each redshift interval represents the best-fit template to CANDELS H-band selected galaxies from all five CANDELS fields. The left panel represents the fractions where we allow additional dust extinction on top of that already implicit in the templates. The right panel we only use the templates, without any additional extinction. The dotted blue line represents the fraction of the eleven templates selected to be LAHz. The dotted black line is the sum of the two earliest morphological classes, representing quiescent spheroidal galaxies.

Our sample of local analogs to high- z (LAHz) is defined by fitting spectral templates of local galaxies to H-band selected galaxies in the CANDELS survey (Grogin et al. 2011; Koekemoer et al. 2011), and selecting those templates that provide the best fit to $z \gtrsim 2$ galaxies as candidates of being local analogs.

We use the galaxy templates presented in Brown et al. (2014). This set of templates contains SEDs covering a wavelength range from UV to the mid-infrared for 129 nearby galaxies. The templates span a wide range of morphologies and galaxy luminosities; they include ellipticals, lenticulars, spirals, as well as irregular and dwarf galaxies. The sample also contains gravitationally interacting galaxies in various stages of mergers, galaxies with an AGN, and luminous infrared galaxies. The templates combine ground-based optical spectroscopy with near and mid-infrared spectroscopy from *Spitzer* and *AKARI*. The wavelength coverage is not contiguous and gaps are filled in using MAGPHYS (Multi-wavelength Analysis of Galaxy Physical Properties code) modeling (da Cunha et al. 2008). The spectral energy distribution from different spectral inputs is normalized and verified with 26 bands of matched-aperture photometry. This allows the mitigation of systematic errors, such as scattered light in IRAC images and errors in the pre-launch *WISE* W4 filter curve (see Brown et al. 2014 for details).

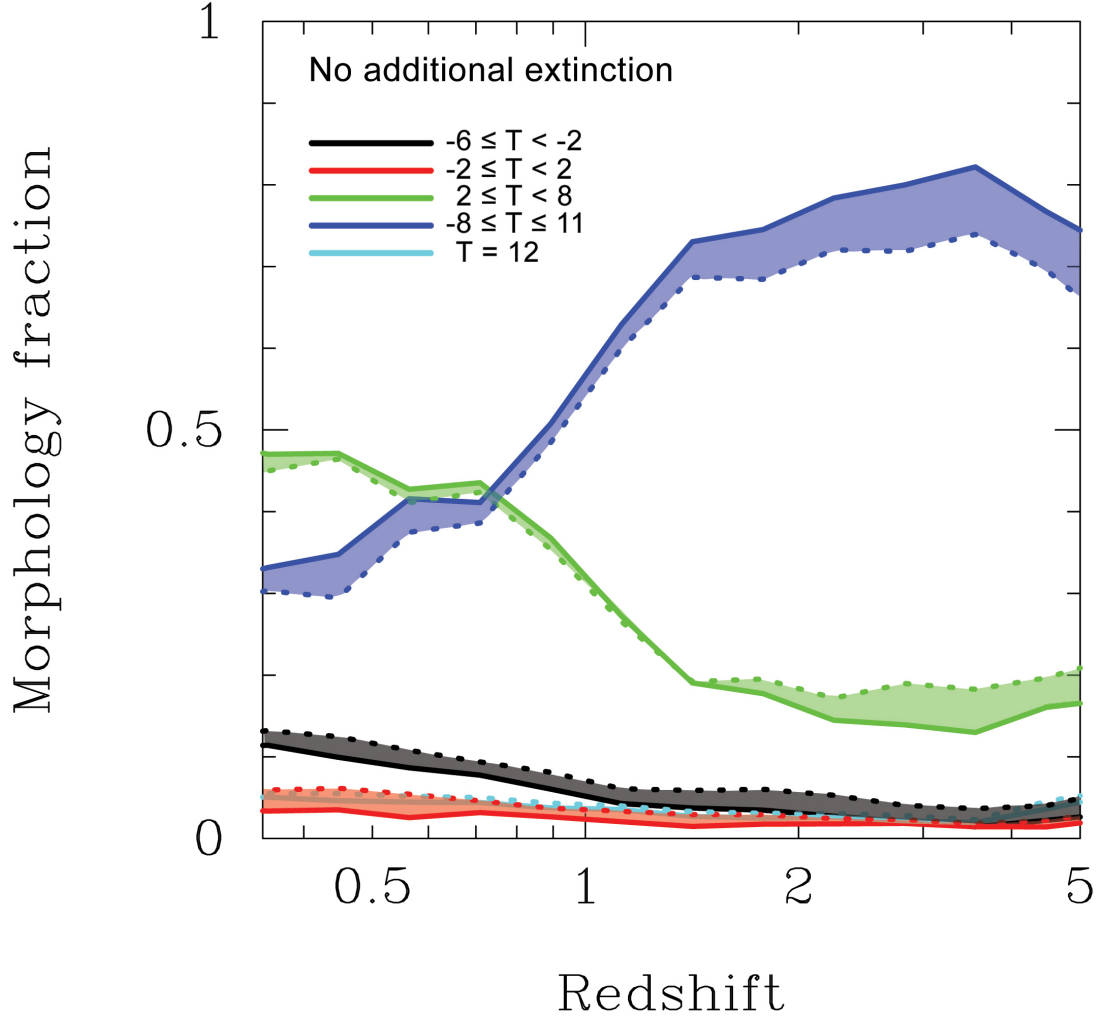


Figure 2. Similar to Figure 1. Here the dashed lines correspond to the best-fit SED to CANDELS galaxies when selecting those with $\Delta\chi^2 = 3$ relative the best-fit SEDs shown in Figure 1 (shown as full drawn lines). The fraction of irregular galaxies decreases slightly, while the fraction of spiral disk galaxies increases. The overall dominance of irregular galaxies in the best-fit SEDs is, however, retained.

For the purpose of establishing which type of templates provide the best-fit SEDs to the high redshift galaxies, we divide the 129 templates into four T-class groups (de Vaucouleurs et al. 1991) : $-6 \leq T < -2$, $-2 \leq T < 2$, $2 \leq T < 8$, $8 \leq T \leq 11$. These four groups correspond to spheroidal, bulge dominated, star forming disks, and star forming irregular galaxies. Galaxies without a designated morphology class, are put in T-class 12, peculiar galaxies. The number of templates in the four main groups are 22, 24, 44, and 20, respectively. In addition, the $T = 12$ peculiar group contains 19 templates.

2.1. High redshift data

The Brown et al. (2014) templates are used to fit to the photometry of high redshift galaxies from the Cosmic Assembly Near-infrared Deep Extragalactic Legacy Survey (CANDELS). CANDELS is a treasury program on Hubble Space Telescope (HST), and provide deep multi-wavelength imaging data in five legacy deep fields: GOODS-South, GOODS-North, UDS, COSMOS and EGS (Grogin et al. 2011; Koekemoer et al. 2011). In this study we use H-band selected catalogs from all five fields. Details on the data and photometry at different wavelength bands are given for;

Table 1. Properties of the local analogs

No.	GALAXY NAME	RA J2000.0	Dec	D Mpc	$\log M_*$ ^(a) M_\odot	$\log M_{HI}$ ^(b) M_\odot	f_{gas} ^(c) M_\odot	Metallicity ^(d) $12 + \log(O/H)$	Alternative Name
1	NGC 2537	08:13:14.4	+45:59:13	8.6	9.02	8.43	0.17	8.19	Arp 6; ‘Bear Paw’
2	Mrk 140	10:16:28.3	+45:19:18	27.6	8.60	8.90	0.56	8.30	Mrk 140
3	Haro 02	10:32:31.9	+54:24:02	23.7	9.21	8.03	0.02	8.45	Mrk 033
4	Mrk 1450	11:38:35.6	+57:52:27	14.7	7.27	7.35	0.54	7.96	
5	UM 461	11:51:33.1	-02:22:22	20.7	7.37	8.47	0.96	7.78	
6	Mrk 1307	11:52:37.4	-02:28:09	21.0	8.07	8.73	0.81	7.96	UM 462
7	Haro 06	12:15:18.4	+05:45:39	35.1	8.58	8.83	0.69	8.18	
8	NGC 4670	12:45:17.1	+27:07:31	20.0	9.38	9.02	0.37	8.30	Arp 163
9	Mrk 475	14:39:05.5	+36:48:21	10.9	6.95	6.62	0.56	7.93	
10	UGCA 410	15:37:04.2	+55:15:48	10.5	7.26	7.58	0.57	8.10	Mrk 487
11	Mrk 930	23:31:58.6	+28:56:50	77.5	8.89	9.51	0.74	8.08	

(a) *Stellar mass* M_* This work. (b) *HI* data from Paturel et al. (2003), except for Mrk 1450 (van Driel et al. (2016)). (c) *Gas fraction* is defined as $f_g = M_g/(M_g + M_*)$. (d) *Metal Abundances* UM 461 and UM 462 (Campos-Aguilar et al. (1993)), Haro 02 (Davidge (1989)).

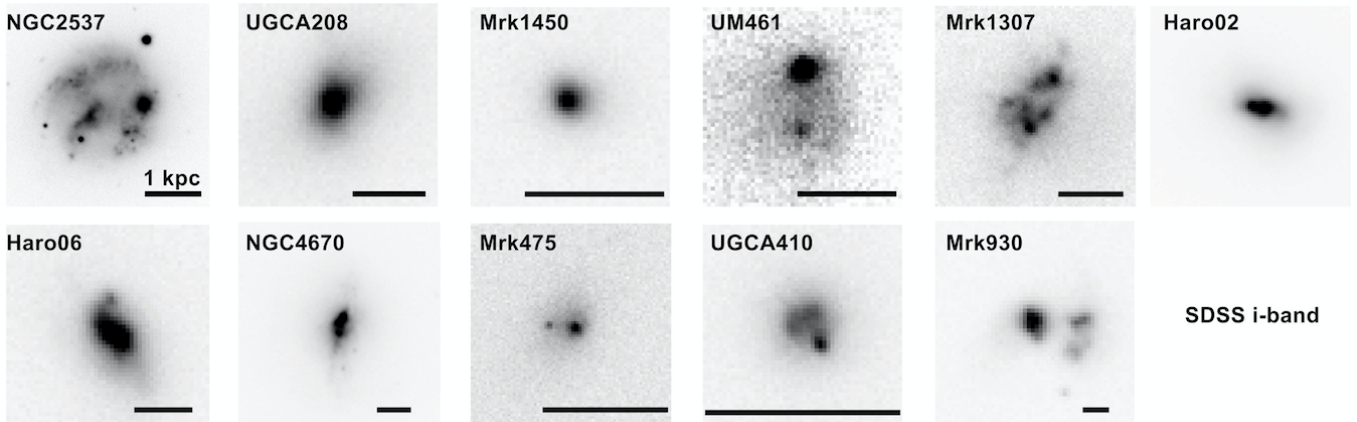


Figure 3. SDSS *i*-band images of our sample. All these galaxies are classified as blue compact dwarf galaxies. The bar corresponds to 1 kpc.

GOODS-S (Guo et al. 2013; Santini et al. 2015), GOODS-N (Barro et al. 2019), UDS (Galamez et al. 2013 ; Santini et al. 2015), COSMOS (Nayyeri et al. 2017), and EGS (Stefanon et al. 2017).

The CANDELS catalogs contain photometric data from the UV to near- and mid-infrared wavelengths, observed in broad, medium, and in some cases, narrow band filters. The catalogs also contain derived physical parameters, such as photometric redshift, stellar mass and star formation rates, compiled using several different teams applying different SED methods, star formation histories and different templates (e.g. Dahlen et al. 2013; Mobasher et al. 2015; Santini et al. 2015). The optical (HST/ACS) and near-IR (HST/WFC3) data are consistently combined with the mid-IR data (*Spitzer*/IRAC) and ground-based observations (UV and K-band). All of the photometric catalogs were selected in the HST/WFC3 F160W band using SExtractor (Bertin & Arnouts 1996). The catalogs for the five different CANDELS fields contain a total of 185,956 galaxies. The number of photometric bands range from 18 (GOODS-S) to 42 (CANDELS COSMOS). The latter catalog includes extensive narrow- and medium-band photometric bands. The mid-infrared data are from *Spitzer*/IRAC (Ashby et al. 2013).

2.2. SED fitting

All 129 of the [Brown et al. \(2014\)](#) templates are used in the SED fitting of the 185,956 CANDELS galaxies. The fits are done in two different modes: keeping the extinction equal to the intrinsic dust extinction of the templates, and allowing additional extinction on top of the intrinsic. The additional extinction is parametrized through the $E(B - V)$ color index. When treated as a free parameter, we allowed additional dust extinction up to $E(B - V) = 0.6$. We use the [Calzetti et al. \(2000\)](#) attenuation law for the additional extinction. An initial test was done keeping the photometric redshift as a free parameter. The redshifts from the SED fits were similar to those presented in the CANDELS catalogs. For the remainder of the analysis, we keep the redshift fixed at the CANDELS values, which includes spectroscopic redshifts whenever available.

The SED fitting procedure involved redshifting the template to the redshift of each galaxy, then each galaxy template is convolved with the filter response functions appropriate for a given CANDELS data set. The template is then fitted to the observed flux densities using χ^2 minimization. If additional extinction is included, we repeat this process for $E(B - V)$ values ranging from 0.0 to 0.6, in steps of 0.01.

We divide the CANDELS galaxies into 13 redshift bins between $0.3 \leq z \leq 5$ ($\Delta z = 0.36$). The total number of galaxies in each redshift bin range from $\sim 2,000$ at $z \sim 0.3$ to $\sim 10,000$ at $z \sim 2$. For each redshift bin we derive the number of best-fit SEDs for each morphological group as defined above. In [Fig. 1](#) we plot the fraction of best-fit SEDs for the four morphological classes as a function of redshift. From the figure it is clear that the Irregular class ($6 \leq T \leq 11$), provides about 35% of the best-fit templates at $z \sim 0.3$, and increase to dominate at $z \gtrsim 1$. At $z \gtrsim 2$, these templates account for 85-90% of all best-fit templates. Of the 20 templates in the $6 \leq T \leq 11$ morphological class, 11 of them provide the most frequent best-fit SED (dotted line in [Fig. 1](#)). These 11 galaxies are selected as our sample of potential Local Analog candidates.

In order to test the robustness of the morphological fractions shown in [Fig. 1](#), we selected the template galaxy with $\Delta\chi^2_\nu = 3$ relative to the best-fit SED. The resulting morphological fraction as a function of redshift is shown in [Fig. 2](#). At $z \gtrsim 1.5$, the fraction of the $6 \leq T \leq 11$ morphological class decreases slightly, while the fraction of star forming spiral disks increases. However, the overall dominance of irregular galaxies as the best templates for high redshift galaxies remains. This shows that the result is robust and local templates with T-class morphologies corresponding to irregular star forming galaxies are best at fitting the SED of high redshift galaxies at $z \gtrsim 1$.

This result is not surprising as galaxies in the $6 \leq T \leq 11$ morphological class share many properties with star forming galaxies at high redshift (e.g. [Elmegreen et al. 2009](#); [Elmegreen et al. 2012](#)). The general properties of the 11 candidates are summarized in [Table 1](#); they have small physical sizes (1 – 2 kpc), they are actively forming stars, and they typically have a high gas mass fraction. Their gas-phase metallicity is low, with an average metallicity of $12 + \log O/H = 8.11 \pm 0.20$, or $\sim 0.26 Z_\odot$. In [Fig. 3](#) we show the Sloan Digital Sky Survey (SDSS) i-band images of the 11 candidates. From these images it is clear that they have irregular morphology with prominent star forming clumps.

All 11 galaxies fall under the classification of Blue Compact Dwarf Galaxies (BCDGs; e.g. [Sargent et al. 1970](#); [Kunth et al. 1988](#); [Thuan & Izotov 2005](#)). BCDGs have previously been proposed to be analogs of high redshift galaxies (e.g. [Hoopes et al. 2007](#)). As a group they share many properties, such as small sizes, clumpy and intense star formation. They show strong optical emission lines, often exhibiting high excitation ([Thuan & Izotov 2005](#)). There are, however, differences among the BCDGs; some show the star forming regions superposed on faint extended stellar emission, suggesting star formation extended over longer time periods (e.g. [Noeske et al. 2003](#)), while others seems to be truly young systems (e.g. [Hunt et al. 2014](#), [Papaderos et al. 2008](#)). The gas-phase metallicities can range from extremely low, like SBS 0335-052E and IZw18, with $Z \approx 0.03$ [Izotov et al. \(2005\)](#), to $Z \approx 0.3 Z_\odot$. One feature that most BCDGs share is the presence of dust. Even the low-metallicity systems SBS 0335-052E and IZw18 show thermal dust emission, even when detectable CO emission is absent ([Hunt et al. 2014](#)). In the remainder of this paper we will characterize the dust emission and the star formation history of the 11 Local Analog candidates defined above, to see whether they can be viewed as scaled down versions of high redshift galaxies.

3. DATA

In this section we describe the data reduction process we used to produce maps of our target galaxies, and the methods to obtain photometric estimates.

In order to characterize the 11 nearby galaxies that make up our sample of potential local analogs, we compile broadband photometric data, covering UV to FIR. We supplement the existing UV-NIR photometric data from [Brown et al. \(2014\)](#) with FIR observations of five galaxies in our sample using the Stratospheric Observatory for Infrared Astronomy

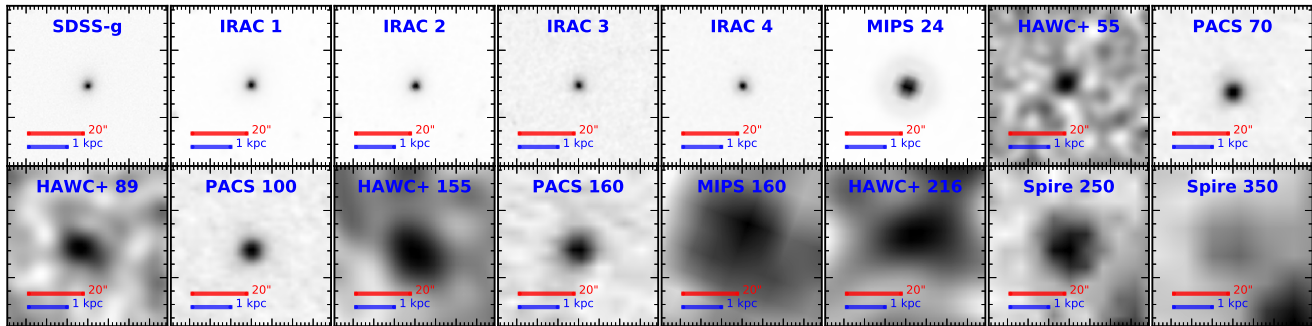


Figure 4. Optical to far-infrared images of Mrk 1450. The red bar corresponds to $20''$, and the blue bar indicates 1 kpc.

Table 2. Multi-wavelength data set¹

GALAXY		FIR PHOTOMETRIC DATA (μm)														
No	NAME	12-22	24-25	55	60	65	70	89-90	100	140-155	160	214	250	350	500	
1	NGC 2537	W	M	S	I	-	M	S	I	S	M	-	-	-	-	
2	Mrk 140	W	M	-	I	-	H	-	H	-	H	-	H	H	H	
3	Haro 02	W	M-I	-	I	-	H	-	H	-	H	-	H	H	H	
4	Mrk 1450	W	M	S	-	-	H	S	H	S	H	S	H	H	H	
5	UM 461	IRS16 - W	M	-	I	-	H	-	H	-	H	-	H	H	H	
6	Mrk 1307	W	M	S	I	-	M	S	I	S	M	-	-	-	-	
7	Haro 06	W	M	S	I	-	H	S	H	S	H	S	H	H	H	
8	NGC 4670	W	M	S	I	-	M	S	I	S	M	S	-	-	-	
9	Mrk 475	IRS16 - W	M	-	-	-	M	-	-	-	M	-	-	-	-	
10	UGCA 410	IRS16	M-I	-	I	A	-	A	-	-	A	-	-	-	-	
11	Mrk 930	W	M	-	-	-	H	-	H	-	H	-	H	H	H	

¹W stands for *WISE*, IRS is for Infrared Spectrograph of *Spitzer*, M for MIPS, S for SOFIA, H for *Herschel* and I for *IRAS*, A for *AKARI*.

(SOFIA). We combined these with archived infrared data from *Herschel*, *Spitzer*, *AKARI*, and *WISE*. A listing of the infrared data sets used in our analysis, indicating the different telescope and instrument combinations, is given in Table 2. In Figure 4 we show an example of imaging of one of our galaxies, Mrk 1450. The images shown consist of our SOFIA-HAWC+ observations, along with archival data from *Spitzer* and *SDSS* band-g (Sloan Digital Sky Survey Gunn et al. 2006) and *Herschel* PACS and SPIRE instruments. Mrk 1450 is well-detected in all bands, but starts to fade in the SPIRE $350 \mu\text{m}$ band, and is undetected in the SPIRE $500 \mu\text{m}$ band.

3.1. SOFIA Observations

The Stratospheric Observatory for Infrared Astronomy (SOFIA: Young et al. 2012, Temi et al. 2014) is a partnership between NASA and the German Aerospace Center (DLR), consisting of an extensively modified Boeing 747SP aircraft carrying a 2.7-meter (106 inch) reflecting telescope (with an effective diameter of 2.5 meters or 100 inches). We were granted ~ 8 hours of observing time with SOFIA; on Cycle 6 under the program 06-0222 (PI: T. Wiklind). We observed 5 galaxies of our sample, using the High-resolution Airborne Wideband Camera-plus instrument (HAWC+; Vaillancourt et al. 2007; Dowell et al. 2010; Harper et al. 2018), covering all available filters to derive the far infrared spectral energy distribution.

The HAWC+ instrument has 5 bands identified as A, B, C, D and E. We observed in bands A, C, D, and E at 53, 89, 154 and $214 \mu\text{m}$, which have beam sizes (full width at half maximum, FWHM) of $4.85''$, $7.80''$, $13.6''$ and $18.2''$ respectively. Band B, was not available during Cycle 6. The galaxies Mrk 1450, NGC 4670, and Haro 06 were observed in all 4 bands available. Due to time constraints, Mrk 1307 and NGC 2537 were only observed at 53, 89, and $155 \mu\text{m}$

bands. The data was reduced to obtain the total intensity maps using the HAWC+ Data Reduction Pipeline v1.3.0 as detailed in Harper et al. (2018).

Table 3. UV - FIR Photometric Data¹

GALAXY NAME	HAWC+A 55 μm	MIPS 60 μm	HAWC+C 89 μm	PACS 100 μm	HAWC+D 155 μm	HAWC+E 214 μm	SPIRE 250 μm
NGC 2537	1302.4 \pm 255.0	4040.0 \pm 286.4	4893.3 \pm 914.1	-	6301.9 \pm 1085.0	-	-
MRK 140	-	-	-	563.2 \pm 44.8	-	-	172.0 \pm 26.3
Haro 02	-	-	-	5051.3 \pm 254.6	-	-	911.9 \pm 137.2
MRK 1450	274.8 \pm 41.6	-	317.0 \pm 47.9	272.0 \pm 21.8	168.2 \pm 27.4	52.5 \pm 17.3	48.7 \pm 8.4
UM 461	-	-	-	132.0 \pm 12.7	-	-	23.1 \pm 7.1
MRK 1307	724.7 \pm 119.9	1000.0 \pm 71.6	1277.6 \pm 198.6	-	616.5 \pm 115.4	-	-
Haro 06	646.3 \pm 97.0	-	849.4 \pm 127.4	742.3 \pm 39.2	754.3 \pm 115.9	309.8 \pm 48.7	197.3 \pm 30.0
NGC 4670	1428.2 \pm 246.1	3470.0 \pm 245.7	3505.9 \pm 530.7	-	3531.9 \pm 713.4	2486.7 \pm 428.9	-
MRK 475	-	110.0 \pm 16.0	-	-	-	-	-
UGCA 410	-	-	-	-	-	-	-
MRK 930	-	-	-	1140.0 \pm 91.9	-	-	210.4 \pm 31.9

¹This is an abbreviated version of the complete table of flux values used for the analysis. The complete table is available in machine readable form in the digital version of this paper. The full table contains 49 columns, indicating the telescope and instrument/band for each measurement and the uncertainty. Fluxes are given in mJy.

3.1.1. SOFIA/HAWC+Photometry

The HAWC+ data is presented in 5 levels: Level 0 is raw data, Level 1 is the demodulated (chop not subtracted) data, after instrument corrections (flat-fielded, dark-subtracted, bad pixel removed) becomes Level 2, level 3 is obtained after flux calibration and telluric correction, and the combined observations from level 3 produces the level 4 data. More details on the pipeline process can be found in the data handbooks (Gordon et al. 2018).

We started our analysis with level 4 maps in units of Jy/pix, and performed annular photometry using the HIPE environment. A circular aperture, centered on the source emission, gives the flux + background emission; an annular region, free of emission and centered on the inner aperture, provides an estimate of the background. To determine the photometric errors we placed six circular apertures of the same radius as the inner source aperture, at equidistant, flux-free, areas around the source. The average flux of the six apertures (B_{gave}) is then subtracted from the source flux:

$$F_{source} = (f_{tot}) - B_{gave}. \quad (1)$$

As a further test, we estimated the integrated flux using CASA¹, and the built-in two-dimensional gaussian procedure. This produced integrated fluxes very similar to the ones obtained using aperture photometry.

To determine the photometry errors we used 6 photometry apertures around the source, taking care to avoid any other source in the background, then the uncertainty of the measurement was defined as the standard deviation of the background apertures. The total error is computed as the addition on quadrature of the uncertainty of the measurement B_{gstd} plus the absolute calibration error, the absolute calibration percentages are listed in Table 4.

$$F_{unc} = \sqrt{(F_{source} * Abs_{scal})^2 + B_{gstd}^2}. \quad (2)$$

The SOFIA/HAWC+ and photometry measure and uncertainties is shown in Table 3 (the full table is available in machine readable form in the digital version of this paper).

¹ <https://casa.nrao.edu/>

Table 4. Fractional calibration error.

Telescope	Instrument	Abs. Calibration
SOFIA	HAWC+	15%
<i>Herschel</i>	PACS	10%
<i>Herschel</i>	SPIRE	15%
<i>WISE</i>	W1-W4	6%
<i>AKARI</i>	N:60,160,WIDE:S,L	10%
<i>Spitzer</i>	IRS	5%
<i>Spitzer</i>	IRAC	5%
<i>Spitzer</i>	MIPS	5%

3.2. Ancillary UV to MIR data

The Brown et al. (2014) templates contain SEDs covering a wavelength range from UV to the mid-infrared for 129 nearby galaxies. As described in section 2, the SEDs of these templates have been normalized and verified with matched-aperture photometry. They provide accurate photometric data, and since our LAHz sample is drawn from these templates, we use the photometric data as presented in Brown et al. (2014).

3.3. Ancillary FIR Data

Some galaxies in our sample were observed with the *Herschel* Space Observatory, using PACS at 70, 100, and 160 μm , with a FOV of $1.75' \times 3.5'$, and SPIRE at 250, 350, 500 μm with a FOV $4' \times 8'$.

The *Herschel* Dwarf Galaxy survey (Madden et al. 2013; Rémy-Ruyer et al. 2013) provide photometric and spectroscopic FIR data on 50 dwarf galaxies. This survey includes data for some of the galaxies in our survey: Mrk 930, Mrk 1450 and UM 461, which were observed with all bands of both PACS and SPIRE instruments. A limited set of *Herschel* photometric data is available for UGCA 410 (also known as Mrk 140) and Haro 02 (Herschel Science. 2013). See the full Table 3 for a complete listing of the FIR photometric data for our sample. For consistency in our flux estimates, we reduced the available *Herschel* PACS and SPIRE data using the *Herschel* pipeline for total intensity photometric measurements. We used the *Herschel* Interactive Processing Environment HIPE (Ott, S. 2010) with version 7 of the photometric calibration.

3.3.1. *Herschel* Photometry

We use level 2.5 or 3.0 maps for our photometry estimates. These maps are created from a combination of different observations of the same target and have improved S/N levels.

For more detail about *Herschel* products see PACS Data Reduction Guide².

To determine the total intensity in *Herschel* PACS 70, 100, and 160 μm maps, we use the PACS - Photometry Script, which is part of *Herschel* common science system (HCSS) provided in the HIPE environment. We started with the maps: Photometry Color High Pass Filter Map (HPPHPFMAPR) level 2.5 or 3.0, depending of availability. We modified parameters in the algorithm in order to use the optimal aperture radius. The final outputs of the algorithm, are the peak flux in Jy/pix, the flux measured by the aperture photometry in Jy, and the aperture corrected flux in Jy. SPIRE photometry maps can be in two different observation mode: *point source* (psrc) in units of Jy/beam or extended source (extsrc) in units of MJy/sr, and are identified as PSW, PMW, PLW that stands for Photometry-Short/Medium/Long-Wavelength, corresponding to 250, 350 and 500 μm respectively. Here we used the psrcPSW, psrcPMW and psrcPLW level 2.5 maps.

Similarly to PACS, for SPIRE photometry maps, we use the SPIRE Photometry Point Source Script provided within HIPE. This, uses the sourceExtractorSussex extractor task to identify the source, and applies the Color Correction for point sources. The *Herschel* pipeline assumes $\alpha = -1$, we assumed $\alpha = 2.0$.

4. METHODOLOGY

² <http://herschel.esac.esa.int/hcss/pacsDRG>

In this section we describe our modeling approach to characterize the dust continuum and the stellar emission. We use two different methods; modified black-body, and the LIGHTNING fitting package (Eufrazio et al. 2017). Both approaches allow for a determination of the far-infrared luminosity and dust mass for each galaxy. The modified black body models are used to also derive luminosity-weighted, dust temperatures, while the LIGHTNING method allows a determination of the star formation history (Section 4.2).

4.1. Black-body Modeling

The simplest characterization of dust emission is to fit it with a black-body $F_\nu \propto B_\nu(T)$. In a more realistic situation, this is modified by taking the transfer of radiation into account. This can be done by using a so-called modified black-body curve, $F_\nu \propto (1 - \exp(-\tau))B_\nu(T)$. We will use the expression:

$$mBB(T) = \Omega B_\nu(T) \left(1 - \exp \left[- \left(\frac{\lambda_0}{\lambda} \right)^\beta \right] \right), \quad (3)$$

where $B_\nu(T)$ is the Planck function, and Ω the solid angle extended by the emission. The opacity is parametrized as $\tau = (\lambda_0/\lambda)^\beta$, where λ_0 is the wavelength where the optical depth equals unity (e.g. Draine 2006), and the coefficient β represents the opacity spectral index (Kovács et al. 2010). Observationally, β has been derived to be between 1 and 2 (cf. Hildebrand 1983; Casey 2012). Data from the Planck mission provides a robust derivation of β in the Milky Way, leading to $\beta = 1.8 \pm 0.1$ (Planck Collaboration et al. 2011). For extragalactic objects it is common to use β in the range 1.3 – 2.0. Here we will adopt the commonly used value $\beta = 1.5$, and keep it constant in our fits. We did try fitting with different β values, but did not find that it changed our results in any significant way. We also kept the wavelength where the optical depth is unity constant at $\lambda_0 = 100\mu\text{m}$. The two parameters β and λ_0 affects the flux on the long wavelength Rayleigh-Jeans part of the dust SED relative to the short wavelength part; for a fixed dust temperature, an increasing λ_0 leads to a relative increase in the Rayleigh-Jeans part, while an increase in β leads to a decrease of the Rayleigh-Jeans part relative the Wien part of the SED.

When fitting a modified black body curve to flux measurements at $\lambda \gtrsim 60\mu\text{m}$, most galaxies exhibit a mid-infrared excess at wavelengths shorter than $60\mu\text{m}$ (e.g. Casey 2012). This excess can be attributed to the presence of a warmer dust component than the one characterizing the longer wavelengths, or an additional heating source, such as an AGN (cf. Scoville & Kwan 1976). The observed mid-IR emission can be modeled as a power law, with a cut-off wavelength λ_c (cf. Casey 2012), or as second, dust component characterized by a warmer dust temperature. Since we do not expect a significant AGN activity in the dwarf galaxies making up our sample, we will adopt the latter case, and use two modified black body curves, with the same β and λ_0 , but with different dust temperatures. Our dust SED to be fitted to the observed data is then:

$$mBB = \Omega_1 B_\nu(T_1) \left(1 - \exp \left[- \left(\frac{\lambda_0}{\lambda} \right)^\beta \right] \right) + \Omega_2 B_\nu(T_2) \left(1 - \exp \left[- \left(\frac{\lambda_0}{\lambda} \right)^\beta \right] \right). \quad (4)$$

With the opacity spectral index kept fixed at $\beta = 1.5$, and the critical wavelength at $\lambda_0 = 100\mu\text{m}$, the modified black body curve contains four free parameters: two dust temperatures T_1 and T_2 , and two normalization constants containing the solid angle of the source Ω . We use the *Levenberg-Marquardt* fitting algorithm. We explored the fitting using values for the dust opacity coefficient β , ranging from 1.2 – 2.0, and for λ_0 in the range 50 – $200\mu\text{m}$. We found no significant variation in the derived dust temperatures, and we conclude that a fixed $\beta = 1.5$ with $\lambda_0 = 100\mu\text{m}$ is sufficient and the models will be characterized by the temperatures and normalization coefficients.

We employ Bayesian statistics inference in multi-parameter spaces to determine the most probable set of model parameters ϕ , of a model mBB_i in comparison to the data D_i . Bayesian inference is based the Bayes' Theorem, which establish the conditional probability of the parameters ϕ given the data D_i as:

$$p(\phi|D_i) = \frac{p(D_i|\phi) * p(\phi)}{p(D_i)}, \quad (5)$$

where the likelihood of the model is $p(D_i|\phi)$. Then $p(\phi|D_i)$ is the posterior probability, $p(\phi)$ is the priors which is the knowledge we have about the parameters or problem. $p(D_i)$ is used to normalize the posterior probability. The likelihood is assumed to be:

$$p \propto \exp(-\chi^2/2).$$

By maximizing the posterior probability we will determine each ϕ parameters best values for the modified black-body models mBB_i . Since we are assuming a fixed $\beta = 1.5$ and $\lambda_0 = 100\mu\text{m}$ for both components, the ϕ parameters are the temperatures T_1 , T_2 , and normalization constants Ω_1 and Ω_2 . The priors are defined by allowing the ϕ parameters to vary through a very wide range initially, to get a posterior probability and then bayesian analysis allows us to update the knowledge of the probability distribution of the parameters and apply new priors multiplying by flat priors that reduce the range of the parameters space. This allows us to reduce the region covered by the parameter and obtain a better resolution of the parameter grid. Inspection of the marginalized probability distribution of each parameter-space, allows us to determine the appropriate range in which the best set of solutions are located, as well as the most likely value. We can also define the confidence interval for each parameter.

4.1.1. Dust masses

The dust mass can be derived from the flux density of optically thin emission.

$$M_{\text{dust}} = \frac{S_\nu D^2}{\kappa_\nu B_\nu(T_d)}, \quad (6)$$

where, S_ν is the observed flux density, $B_\nu(T_d)$ the black-body emission at a given temperature, D is the distance, and κ_ν is the dust absorption coefficient for dust grains at frequency ν . The dust absorption coefficient is a parameter encompassing both the dust grain composition and the grain size distribution, and is difficult to derive observationally (e.g. Gordon et al. 2014). Weingartner & Draine (2001) derived κ_ν for different R_V values for Milky Way dust. We will use the average κ_ν for $R_V = 3.1, 4.0$ and 5.5 at $\lambda = 250\mu\text{m}$. Using updated values, we have $\kappa_{250} = 0.40 \text{ m}^2 \text{ kg}^{-1}$. We do not have observed flux values at $\lambda = 250\mu\text{m}$ for all of our galaxies. Instead we use the flux density provided by our mBB fits to the overall dust SED.

Hence, the dust mass, using the flux density at $250\mu\text{m}$, can be expressed as:

$$\frac{M_{\text{dust}}}{M_\odot} = 188.4 \left(\frac{S_\nu}{\text{Jy}} \right) \left(\frac{D}{\text{Mpc}} \right)^2 \frac{(\exp(57.55/T) - 1)}{\kappa_{250}}. \quad (7)$$

The dust masses derived in this way are listed in Table 5 and discussed in Section 5.3.

4.2. LIGHTNING SED Fits

We performed SED fitting using LIGHTNING (Eufrazio et al. 2017, ASCL:1711.009³), which fits non-parametric star formation histories (SFHs) in discrete, fixed-width, stellar age bins. We made use of the most recent update to LIGHTNING, which uses an adaptive Markov Chain Monte Carlo (MCMC) algorithm (Doore et al. 2021, in prep). For this work we have used SFH bins of 0–10 Myr, 10–100 Myr, 100 Myr–1 Gyr, 1–5 Gyr, 5–13.3 Gyr, assumed a Kroupa IMF (Kroupa 2001) and a metallicity of $0.2Z_\odot$. We used PEGASE (Fioc & Rocca-Volmerange 1997; Fioc & Rocca-Volmerange 1999) stellar populations. For intrinsic attenuation, we adopted a Calzetti et al. (2000) extinction law, modified as in Noll et al. (2009) to include a UV bump at 2175 \AA and a parameter δ to control the UV slope. Draine & Li. (2007) Milky Way dust emission was used. For a more thorough description of the prescriptions adopted by LIGHTNING, we refer the reader to Eufrazio et al. (2017).

The IR photometry previously described was combined with literature SEDs from Brown et al. (2014), producing SED with 45 data-points from the FUV to the FIR (including GALEX, Swift UVOT, SDSS, 2MASS, WISE, Spitzer, SOFIA, IRAS, AKARI, and Herschel). Our fits explore a 13-dimensional parameter space with 5 parameters regarding the SFH intensities, $\psi_i \geq 0$, 3 parameters ($0 \leq \tau_V^{\text{DIFF}} \leq 3$, $-2.3 \leq \delta \leq 0.4$, and $0 \leq \tau_V^{\text{BC}} \leq 4$) controlling the dust extinction, and 5 dust emission parameters ($0 \leq \alpha \leq 4$, $0.1 \leq U_{\text{min}} \leq 25$, $10^3 \leq U_{\text{max}} \leq 3 \times 10^5$, $0 \leq \gamma \leq 1$, and $0.0047 \leq q_{\text{PAH}} \leq 0.0458$). We run the adaptive MCMC algorithm for 3×10^5 steps and derive statistics from the last 5,000 steps of the chain. All the derived quantities quoted here (SFHs, SFRs, M_\star , M_{dust}) are derived from these last 5,000 steps.

³ <https://github.com/rafaeleufrazio/lightning>

5. RESULTS

We derive properties of the dust in our LAHz galaxies using two different methods. Some of the derived parameters are duplicated in the two methods, such as the FIR luminosity and dust mass. Others are unique for each method. For instance, the modified black body models provide luminosity-weighted dust temperatures, which the LIGHTNING models do not. The LIGHTNING models provide an estimate of the SFR integrated over the last 100 Myr, and a parametrized star formation history (SFH). The derived parameters from the modified back body models are presented in Table 5, and those from the LIGHTNING models in Table 6.

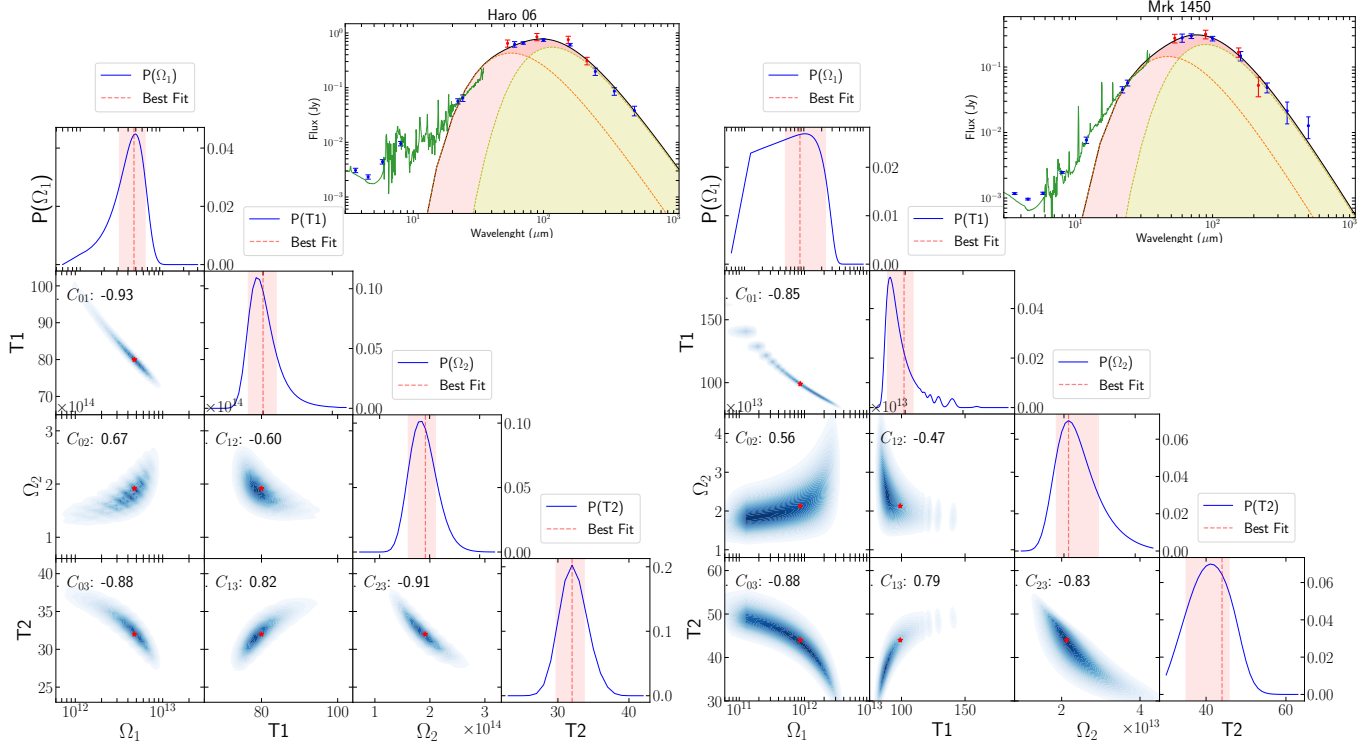


Figure 5. Corner plots for the modified black-body models of the SED of Haro 06 and Mrk 1450. In each panel, in the bottom: The 2D scatter plots (blue area) of the values recovered from the four parameters grid are shown for the two-by-two combination of parameters (two temperatures and two normalization constants). On top are the histograms for all 4 parameters we display Bayesian 1D marginalized likelihoods. The best-fit values to the observed data in the histograms are shown in red and the light-red area encloses 68 % of the likelihood. Top right: Best fit model in black, shows the two dust components, cold component in yellow and warm in light-red. The red are the SOFIA data points, and blue data points are the ancillary data available. The green solid line is the [Brown et al. \(2014\)](#) spectral data, which is not part of the fits, however is in good agreement with the modified black-body model.

5.1. Modified Black-Body models

The black-body modeling described in section 4.1 show that a reasonable description of the dust SED can be achieved by using a two-component modified black-body fit. The warm component is less well constrained than the cold component due to a smaller number of photometric data points at wavelengths $\lambda \lesssim 60\mu\text{m}$. Nevertheless, the model SED joins smoothly with the near- and mid-IR fluxes of the [Brown et al. \(2014\)](#) templates.

In Figure 5 we show multi-parameter-space diagnostic plots for two galaxies in our sample: Haro 06 and Mrk 1450. We can see the marginalized distribution for each ϕ parameter in the upper frame of each column, the lower frames show the marginalized probability in blue and the correlation values between each two parameters. The value that maximizes the χ^2 distribution (likelihood) for each parameter is indicated with a red star; this is also shown as a red

dashed line in the upper frames for each parameter. The confidence interval is shown in light red and indicates the 16 and 84 percentiles in the probability distribution, which imply that the 68% of the probability is inside that region.

This visualization of the probability distributions allow us to understand how the different parameter relate. For instance we can see how the temperature T_1 and the constant Ω_1 are anti-correlated, while the two constants Ω_1 and Ω_2 are positively correlated for both galaxies. In the upper right box we see the best fit model indicating the two black-body components representing a warm and a cold dust component. The corresponding [Brown et al. \(2014\)](#) template is shown as a reference, but it is not part of the fit. The resulting best-fit model agrees smoothly with the Brown templates.

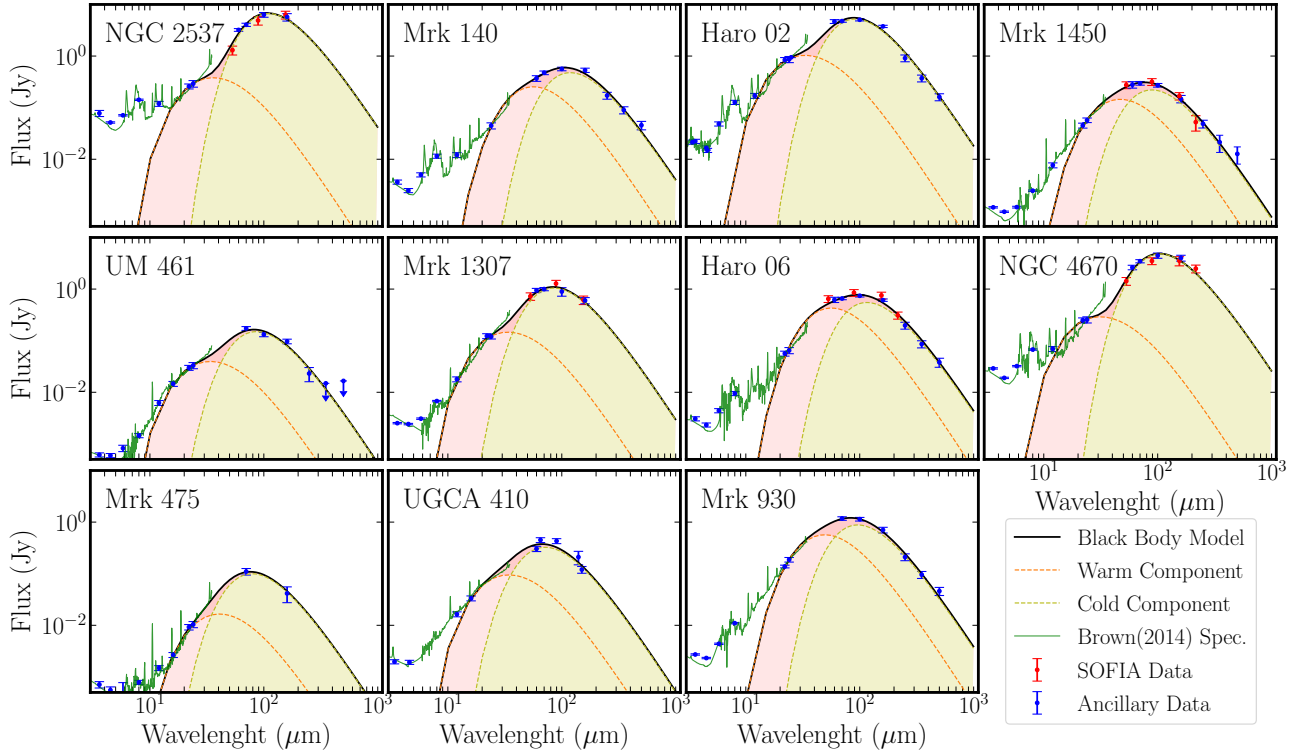


Figure 6. Black-body best fits: LAHz dust emission. The best modified black-body fit shown in black solid line, the light-green and light-red dash lines are the warm and cold components. SOFIA (53, 89, 155, 216 μm) data points in red, ancillary data points in blue *Herschel* (60, 100, 160, 250, 350, 500 μm) data points and *Spitzer*-MIPS (24, 60, 100, 160 μm) in blue where used when SOFIA or *Herschel* data was not available in the corresponding band. The green solid line is the [Brown et al. \(2014\)](#) spectra templates, plotted as a reference, which are not part of the black-body fits.

In Figure 6 we present the SEDs, produced by the two-component black-body models for all of our LAHz. In a few cases the warm and the cold components show a double-peaked SED often found for star-forming spiral galaxies. However, in several cases, the warm and cold components blend together and form a broad single-peaked SED. In the figures we also include the corresponding NIR and MIR spectra from [Brown et al. \(2014\)](#). These spectra were not part of the fit, but they merge smoothly with the dust SED. In three cases (NGC 2537, Haro 02 and NGC 4670), the MIR spectra suggest that there might be additional flux at wavelengths between 24 μm and 70 μm , than what is indicated in the two-component black-body fits.

5.1.1. Dust temperatures

We obtained the dust temperatures characterizing the warm and cold components from the modified black-body fits. For comparison we use the Dwarf Galaxy survey presented by [Rémy-Ruyer et al. \(2013\)](#) which includes local dwarf galaxies, and, in order to provide a comparison with more evolved galaxies, we use a subset of 58 galaxies from the

Table 5. Modified Black-Body Derived Quantities

NO	GALAXY NAME	T_{dWarm} K	T_{dCold} K	$S_{24\mu m}/S_{160\mu m}^I$	M_d M_\odot	L_{FIR} $10^9 L_\odot$
1	NGC 2537	139.0^{+70}_{-16}	$34.0^{+0.9}_{-1.5}$	0.06	$3.83^{+0.7}_{-0.8} \times 10^5$	0.638 ± 0.028
2	Mrk 140	79.0^{+5}_{-7}	$31.0^{+1.0}_{-3.6}$	0.10	$4.05^{+1.1}_{-0.5} \times 10^5$	0.784 ± 0.043
3	Haro 02	153.0^{+8}_{-29}	$42.5^{+0.8}_{-1.6}$	0.29	$9.53^{+0.7}_{-1.0} \times 10^5$	6.222 ± 0.172
4	Mrk 1450	100.0^{+37}_{-9}	$44.0^{+5.3}_{-4.5}$	0.41	$1.36^{+0.2}_{-0.3} \times 10^4$	0.150 ± 0.008
5	UM 461	148.0^{+8}_{-15}	$46.0^{+2.5}_{-3.8}$	0.42	$1.55^{+0.4}_{-0.3} \times 10^4$	0.161 ± 0.009
6	Mrk 1307	149.0^{+1}_{-40}	$46.0^{+0.9}_{-4.2}$	0.23	$1.12^{+0.4}_{-0.2} \times 10^5$	0.913 ± 0.038
7	Haro 06	79.0^{+10}_{-2}	$32.0^{+3.1}_{-1.6}$	0.14	$6.67^{+0.6}_{-1.4} \times 10^5$	1.809 ± 0.092
8	NGC 4670	162.0^{+13}_{-51}	$36.0^{+0.4}_{-2.5}$	0.08	$1.19^{+0.3}_{-0.2} \times 10^6$	2.665 ± 0.109
9	Mrk 475	119.0^{+8}_{-11}	$51.0^{+4.3}_{-8.6}$	0.24	$1.96^{+1.6}_{-0.7} \times 10^3$	0.024 ± 0.003
10	UGCA 410	146.0^{+29}_{-10}	$58.0^{+5.8}_{-4.7}$	0.71	$3.71^{+0.9}_{-1.0} \times 10^3$	0.103 ± 0.006
11	Mrk 930	94.0^{+6}_{-14}	$40.0^{+1.4}_{-8.3}$	0.29	$2.18^{+0.7}_{-0.3} \times 10^6$	16.225 ± 1.313

¹The flux ratio $S_{24\mu m}/S_{160\mu m}$ is derived from the modified black-body best fit model.

Table 6. LIGHTNING-Derived Quantities

No.	GALAXY NAME	M_{dust} $10^4 M_\odot$	L_{FIR} $10^9 L_\odot$	M_* $10^8 M_\odot$	SFR^I $M_\odot \text{ yr}^{-1}$	sSFR Gyr^{-1}
1	NGC 2537	9.5 ± 3.0	$0.77^{+0.02}_{-0.02}$	$10.5^{+1.3}_{-1.4}$	$0.20^{+0.04}_{-0.04}$	0.19 ± 0.04
2	Mrk 140	25.7 ± 7.2	$0.94^{+0.03}_{-0.03}$	$3.9^{+0.5}_{-0.5}$	$0.18^{+0.05}_{-0.05}$	0.46 ± 0.14
3	Haro 02	21.5 ± 4.8	$8.03^{+0.21}_{-0.20}$	$16.3^{+2.2}_{-2.2}$	$1.3^{+0.4}_{-0.3}$	0.80 ± 0.23
4	Mrk 1450	1.9 ± 0.2	$0.19^{+0.01}_{-0.01}$	$0.19^{+0.03}_{-0.02}$	$0.03^{+0.01}_{-0.01}$	1.60 ± 0.44
5	UM 461	1.3 ± 0.3	$0.21^{+0.01}_{-0.01}$	$0.21^{+0.03}_{-0.02}$	$0.03^{+0.01}_{-0.01}$	1.17 ± 0.50
6	Mrk 1307	11.0 ± 2.9	$1.10^{+0.04}_{-0.04}$	$1.2^{+0.2}_{-0.2}$	$0.29^{+0.05}_{-0.04}$	2.51 ± 0.55
7	Haro 06	81.8 ± 5.8	$2.18^{+0.06}_{-0.06}$	$3.8^{+0.8}_{-0.7}$	$0.70^{+0.06}_{-0.06}$	1.83 ± 0.40
8	NGC 4670	207.0 ± 66.0	$3.30^{+0.1}_{-0.1}$	$24.2^{+1.9}_{-2.1}$	$0.19^{+0.07}_{-0.06}$	0.08 ± 0.03
9	Mrk 475	0.17 ± 0.04	$0.028^{+0.002}_{-0.002}$	$0.09^{+0.01}_{-0.01}$	$0.003^{+0.002}_{-0.001}$	0.39 ± 0.20
10	UGCA 410	2.6 ± 1.2	$0.15^{+0.01}_{-0.01}$	$0.18^{+0.04}_{-0.03}$	$0.04^{+0.01}_{-0.01}$	2.21 ± 0.64
11	Mrk 930	68.7 ± 19.5	$19.1^{+0.7}_{-0.7}$	$7.7^{+1.3}_{-1.1}$	$3.6^{+0.4}_{-0.4}$	4.71 ± 0.87

¹The star formation rate averaged over the last 100 Myrs.

Key Insights on Nearby Galaxies: a Far- Infrared Survey with *Herschel* (KINGFISH Kennicutt et al. 2011), where we exclude the irregular dwarf galaxies and early type galaxies from the original set of 109 galaxies.

In order to compare our results with the galaxies in the DGS and KINGFISH samples, we re-analyzed the FIR photometric data from these surveys using the same modified black body method as for our LAHz galaxies. For each galaxy we derive the temperatures characterizing the warm and cold components, as well as the temperature

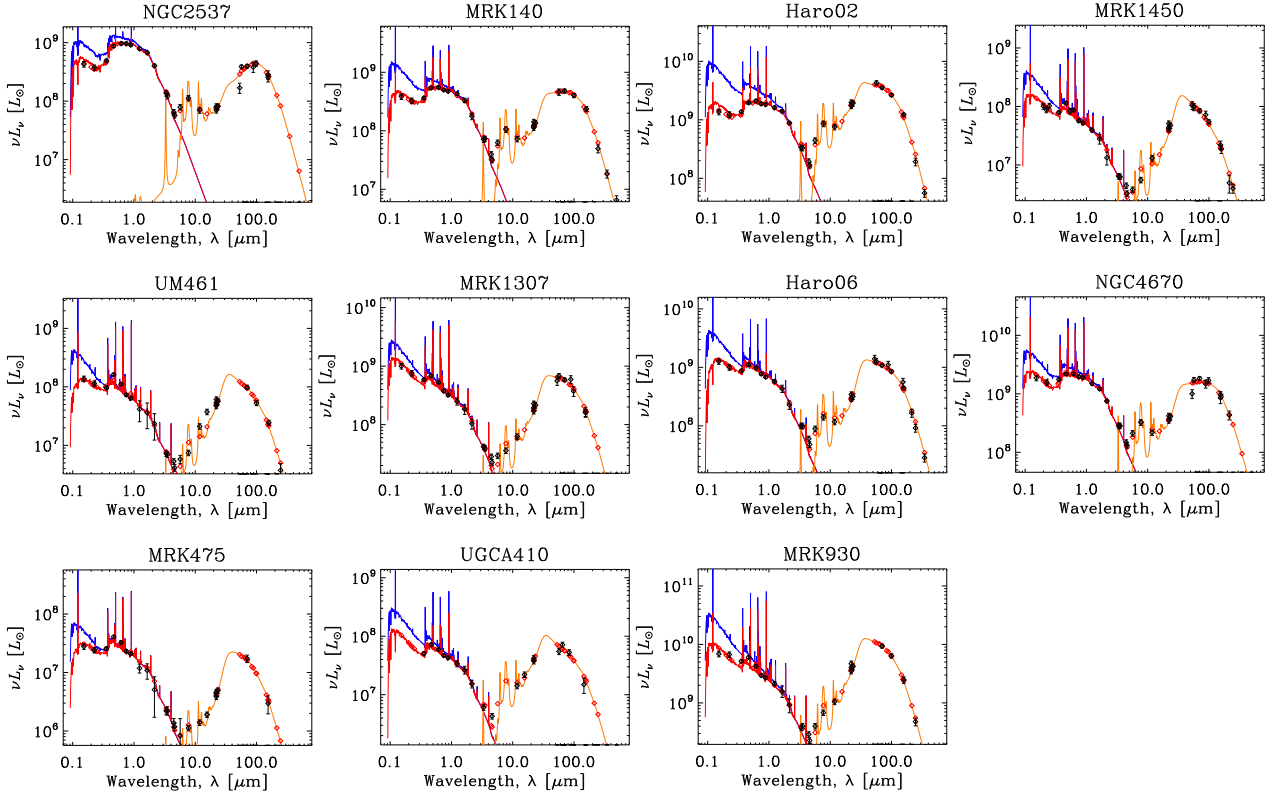


Figure 7. FUV-to-FIR SEDs produced with the LIGHTNING fitting package. Intrinsic stellar spectra are shown in blue. Attenuated stellar spectra are shown in red. Dust emission spectra are shown in orange. The observed data are shown as black diamonds. Red diamonds are the model SEDs, i.e., the attenuated stellar spectra plus the dust emission spectra convolved with the filter functions. When no observations are available in a band, models are still computed.

corresponding to the peak of the combined SED, defined as:

$$T_{\text{peak}} = \frac{b}{\lambda_{\text{peak}}}, \quad (8)$$

where b is the Wien’s displacement constant. All the galaxies were characterized using two dust components. The average dust temperatures for the sample of LAHz are $T_{\text{d, warm}} \sim 124$ K, and $T_{\text{d, cold}} \sim 42$ K. This is significantly higher than for star-forming disk galaxies in the KINGFISH sample, with $T_{\text{d, warm}} \sim 68$ K and $T_{\text{d, cold}} \sim 23$, and higher than for the DGS sample with $T_{\text{d, warm}} \sim 74$ K and $T_{\text{d, cold}} \sim 24$. The range of temperatures for the DGS survey for the cold component is, however, quite large, ranging from 18 – 41 K (Rémy-Ruyer et al. 2013). The results are shown in Figure 9.

5.2. LIGHTNING models

As described in Sect.4.2, the LIGHTNING models fit the whole UV-FIR SED, while self-consistently applying an extinction correction. The FIR is modeled using Draine & Li. (2007) templates. The resulting SEDs for our LAHz galaxies are shown in Figure 7. The black data points represent the observed SED; the blue line is the spectra without dust attenuation; the red line is the SED with attenuation; the orange line is the best-fit dust emission. In Table 6 we show luminosities, dust masses, SFR averaged over the last 100 Myrs and specific star formation rates (sSFRs) derived from the LIGHTNING models.

5.3. Far-infrared luminosity and dust mass

We derive dust masses and L_{IR} using the SEDs produced with the two different modeling methods described in Sect. 4. The dust masses and L_{IR} from the mBB models and the LIGHTNING method are presented in Table 5 and Table 6 respectively. The L_{IR} is derived by integrating the SED from $8 \mu\text{m}$ to $1000 \mu\text{m}$. The LAHz galaxies

luminosities cover a wide range of $\log(L_{\text{IR}}/L_{\odot}) = [7.4, 10.2]$ for the black-body models, similarly, the LIGHTNING method luminosities range between $\log(L_{\text{IR}}/L_{\odot}) = [7.5, 10.3]$.

The derived dust masses using the black-body models are in the range of: $\log(M_{\text{dust}}/M_{\odot}) = [3.1, 6.3]$. As expected the cold dust component dominates the total dust mass. We also derive the dust mass from the Draine & Li best fits in the LIGHTNING models: $\log(M_{\text{dust}}/M_{\odot}) = [3.2, 6.3]$. Some of the galaxies in our sample have published dust mass values, derived using a subset of the photometric data used here (e.g. Engelbracht et al. 2008; Rémy-Ruyer et al. 2013), which agree very well with the results presented here. For the discussion presented in the rest of this paper, we use the dust masses derived with the mBB method, since this allows the comparison with dust masses derived for surveys samples like the KINGFISH and DGS using the same methodology.

We compare the dust masses and FIR luminosities for our LAHz galaxies, derived with the modified black body and LIGHTNING methods. The latter method uses the Draine & Li. (2007) templates to model the FIR SED. The dust masses derived from the *mBB* and the Draine & Li models, show dispersion of ~ 0.3 dex, but shows no systematic difference. The FIR luminosities, however, do show a systematic offset, where the Draine & Li. (2007) based models give $\sim 20\%$ higher L_{FIR} than those derived by integrating over the modified black body models. This is expected since the Draine & Li. (2007) models include PAH emission in the near-infrared, and better account for the near- to mid-IR emission than the black body models. In the rest of the paper we will use the *mBB*-derived dust masses for comparison with the DGS and KINGFISH surveys. And the LIGHTNING FIR luminosities for discussions and conclusions.

5.4. Star formation histories

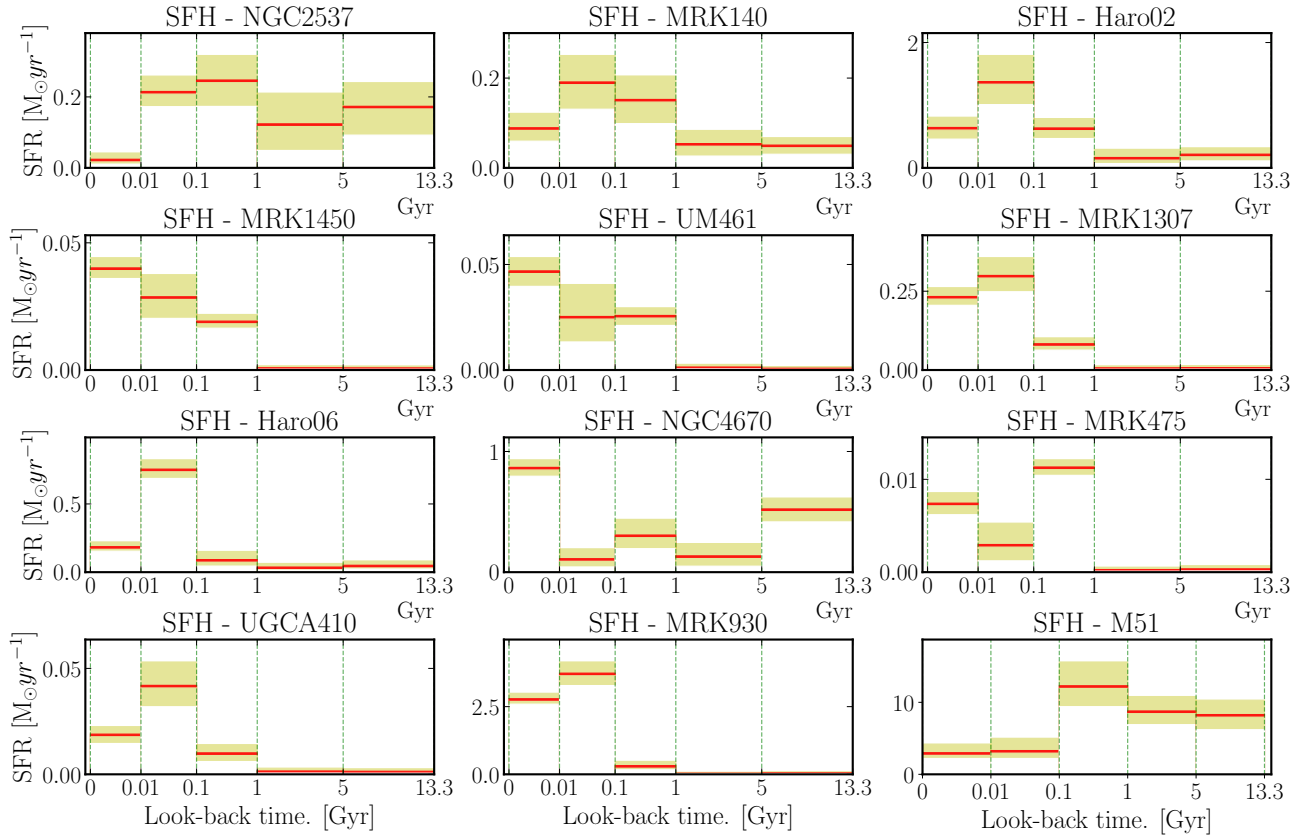


Figure 8. Star formation histories for our sample. The SFHs are divided into five time bins: 0 to 10 Myr, 10 to 100 Myr, 100 Myr to 1 Gyr, 1 to 5 Gyr and 5 to 13.3 Gyr. The solid lines denote the median values from the MCMC chain and dotted lines show the 16th and 84th percentiles, enclosing the hashed areas. For comparison the last frame includes the SFH of M51, derived by Eufraasio et al. (2017), following similar approach.

In Fig. 8 we show the SFH for the LAHz galaxies in our sample. For comparison we also show the SFH of M51 from [Eufrasio et al. \(2017\)](#). The SFH was derived using the LIGHTNING fitting package, and it is presented in 5 look-back time bins: 0 – 10 Myrs, 10 – 100 Myr, 0.1 – 1 Gyr, 1 – 5 Gyr and 5 – 13.3 Gyr. The LIGHTNING modeling treats the SFR as constant over each time bin. The solid red line denote the median SFR for each time bin from the simulations and the yellow region denotes the 16th and 84th percentiles, enclosing the 68% confidence intervals. The SFHs of the LAHz are for the most part very different from those of more massive galaxies. For instance, the SFH of M51, a large spiral galaxy gravitationally interacting with a neighbor galaxy, shows a more complex SFH, with a significant star formation contribution in bins corresponding to ages older than 5 Gyr.

For the LAHz we recover SFHs consistent with null SFR contribution at ages older than 1 Gyr for 6 galaxies: Mrk 1450, UM 461, Mrk 1307, Mrk 475, UGCA 410 and Mrk 930. This suggests that they are the youngest galaxies in our sample. Two of the galaxies, NGC 2537 and NGC 4670, show significant star formation activity in all five time bins, indicating the presence of an old stellar population. Hence, despite being designated as Blue Compact Dwarf Galaxies, the stellar mass of these two galaxies is dominated by old stars. The situation is less clear for three of the galaxies in our sample, Mrk 140, Haro 02 and Haro 06, where the LIGHTNING results indicate that it is probable that they had a low level of star formation activity at times $\gtrsim 1$ Gyr (see Figure 8).

We consider the six LAHz galaxies that have SFHs consistent with being younger than ~ 1 Gyr as our prime candidates for being local analogs. NGC 2537 and NGC 4670 are clearly not young galaxies. Mrk 140, Haro 02 and Haro 06 are likely to have an old stellar population, although Haro 06 is a borderline candidate for being a local analog.

6. DISCUSSION

6.1. Characteristic dust temperatures

When fitting a two-component modified black body curve to our LAHz galaxies, the Dwarf Galaxy Survey and spiral galaxies in the KINGFISH sample, we find that the DGS and LAHz galaxies show a higher T_{peak} than the more massive KINGFISH galaxies (Figure 9). While the average T_{peak} is 33 K and 35 K for the LAHz and DGS samples, respectively, the KINGFISH galaxies have an average of $T_{\text{peak}} = 23$ K. When we compare the warm/cold dust component separately, we see that the LAHz are characterized by higher dust temperatures than both the KINGFISH and the DGS galaxies. These results are consistent with a general trend of warmer dust in metal-poor galaxies compared with the more metal-rich and more massive counterparts (e.g. [Rémy-Ruyer et al. 2013](#)) as well as for high- z galaxies (e.g. [Faisst et al. 2017](#) and [Sommovigo et al. 2020](#)).

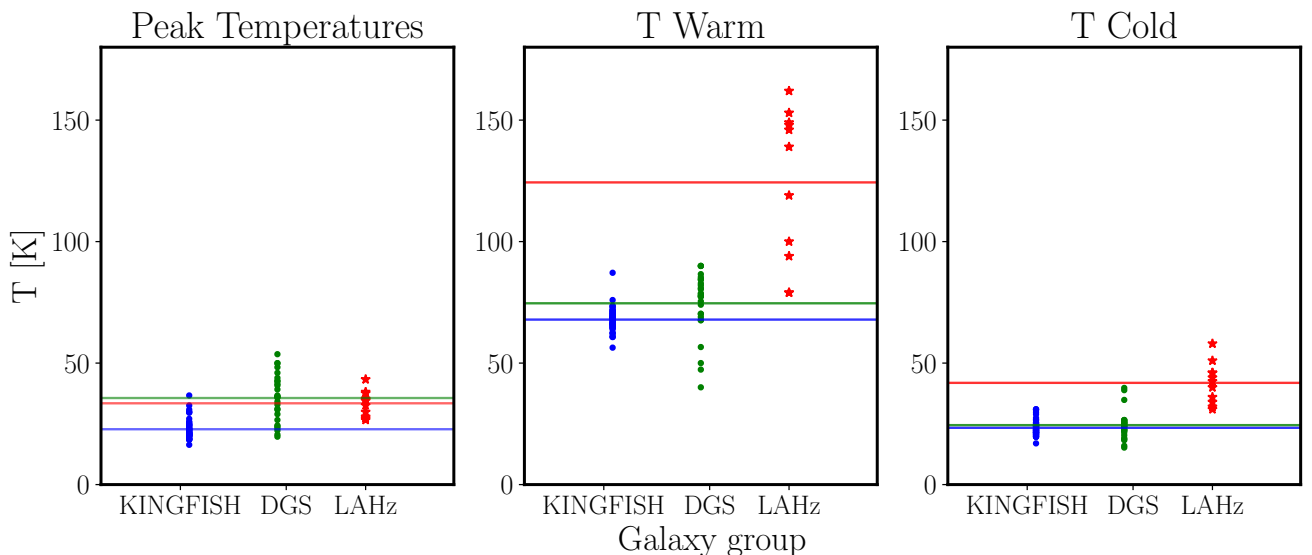


Figure 9. Comparison of peak, warm, and cold temperatures characterizing the dust. Solid lines indicate average temperatures; the dots are the individual values for each galaxy. KINGFISH galaxies are shown in blue, DGS in green, and the LAHz candidates in red. All temperatures were determined using modified black-body procedure (see section 4.1).

6.2. Dust-to-stellar mass ratio

In Figure 10, (top-left frame), we show the dust-to-stellar mass ratio as a function of stellar mass for our sample, together with those of the DGS, and KINGFISH spiral galaxies. While the KINGFISH galaxies seem to have a weak dependence on stellar mass, no such correlation is apparent for our LAHz galaxies or for galaxies in the DGS sample. In fact, the dust-to-stellar mass ratio for the LAHz seems to be approximately constant, with a median ratio $\log(M_{\text{dust}}/M_{\star}) = (8.5 \pm 5) \times 10^{-4}$. A similar argument can be made for the DGS sample, but with a slightly lower average dust to stellar mass ratio. The dashed line shown in Figure 10 shows the anti-correlation between dust-to-stellar mass ratio and stellar mass found by Clemens et al. (2013). This anti-correlation was obtained for galaxies from the Planck Survey and the fit is dominated by galaxies in the stellar mass range $\log M_{\star}/M_{\odot} \sim 10 - 11$. The anti-correlation is surprising in view of the fact that the gas-phase metallicity scales with stellar mass (e.g. Tremonti et al. 2004) and one would expect a lower $M_{\text{dust}}/M_{\star}$ ratio for low-mass galaxies. The Clemens et al. (2013) relation has been interpreted as being due to a rapidly increasing gas fraction for lower-mass galaxies, more than offsetting the metallicity effect. However, the results shown here, both for our sample and that of DGS, show that this relation cannot be extended to low-mass galaxies.

The mass-metallicity relation is established down to $\log M_{\star}/M_{\odot} \sim 8.5$. Below this stellar mass, depletion of metals through galactic winds starts to become important (e.g. Tremonti et al. 2004). Our LAHz galaxies have $\log M_{\star}/M_{\odot}$ in the range 7.0 – 9.4, straddling the $\log M_{\star}/M_{\odot} = 8.5$ value. In Figure 10, top-right panel, we show the relation between the dust-to-stellar mass ratio as function of metallicity. In the figure we also include the DGS and KINGFISH spiral samples. Based on the latter two samples, Rémy-Ruyer et al. (2013) defined a correlation between the dust-to-stellar mass ratio and gas-phase metallicity, shown as a dashed line in Figure 10. We find no obvious correlation between the dust-to-stellar mass ratio and metallicity for our LAHz sample, and the overall dispersion of dust-to-stellar mass ratios is large. As discussed in Rémy-Ruyer et al. (2013), this could at least in part be due to observational uncertainties. However, for the metal-poor, and low-mass galaxies, this could also be due to the impact of individual star formation histories, where the interstellar gas can be promptly enriched through recent star formation, or depleted due to galactic winds. Evidence for both effects have been seen in this type of galaxies; Lagos et al. (2018) found spatial variations in the gas-phase metallicity in UM 461, attributed to recent infall of low-metallicity gas, and Haro 02 shows clear evidence of a galactic gas outflow (e.g. Meier et al. 2001; Beck et al. 2020).

For comparison we also include two of the lowest metallicity galaxies known, SBS 0335-052E and IZw18 in Figure 10. Both of these galaxies have very low gas-phase metallicity, $12 + \log O/H \sim 7.2$, but even at these extremely low metallicities they still show dust continuum emission (SBS 0335-052E: Hunt et al. (2014); IZw18: Wu et al. (2007)). These two particularly low-metallicity galaxies were studied by Hunt et al. (2014), and found to have dust-to-stellar mass ratios within the range of values found for the galaxies presented in Figure 10. The dust-to-stellar mass ratio of IZw18 is $\log(M_{\text{dust}}/M_{\star}) = -3.60$, which is consistent with the LAHz average of $\log(M_{\text{dust}}/M_{\star}) = -3.17$. SBS 0335-052E, however, has $\log(M_{\text{dust}}/M_{\odot}) \approx -2.15$, which is significantly higher than the LAHz and DGS galaxies, comparable with metal-rich spiral galaxies. While this wide disparity among the most metal-poor galaxies could be due to observational uncertainties, it could also be an effect of the above mentioned prompt enrichment and galactic outflow/inflow processes affecting low-mass galaxies.

The bottom-right panel of Figure 10 shows the $L_{\text{IR}}/M_{\text{dust}}$ ratio as a function of metallicity for the LAHz galaxies (red squares). For comparison we also show the DGS and KINGFISH galaxies. The distribution of $L_{\text{IR}}/M_{\text{dust}}$ is indicated on the side for each group. The $L_{\text{IR}}/M_{\text{dust}}$ of the LAHz galaxies is distributed in the same range as the DGS (Rémy-Ruyer et al. 2013). This ratio tends to increase for lower metallicities, and when we examine the left region in the range of metallicities, the LAHz exhibit higher $L_{\text{IR}}/M_{\text{dust}}$ ratio than the DGS or KINGFISH galaxies for the corresponding metallicity. This means that the dust grains in the LAHz sample are more efficient, on average, at radiating far-infrared photons. It is not possible with the present data to determine whether this is due to different grain properties, or is simply an effect of the higher dust temperatures characterizing the dust emission in these galaxies. As shown in Figure 10, this trend extends to the extremely metal-poor galaxies SBS 0335-052E and IZw18, covering more than an order of magnitude in both metallicity and $L_{\text{IR}}/M_{\text{dust}}$. These two galaxies are dominated by warm dust; their single-component dust SEDs are characterized by $T_{\text{dust}} = 59$ and 67 K, respectively (Hunt et al. 2014). While these temperatures are high, they are within the range of the temperatures characterizing our LAHz galaxies.

6.3. Star Formation vs. AGN

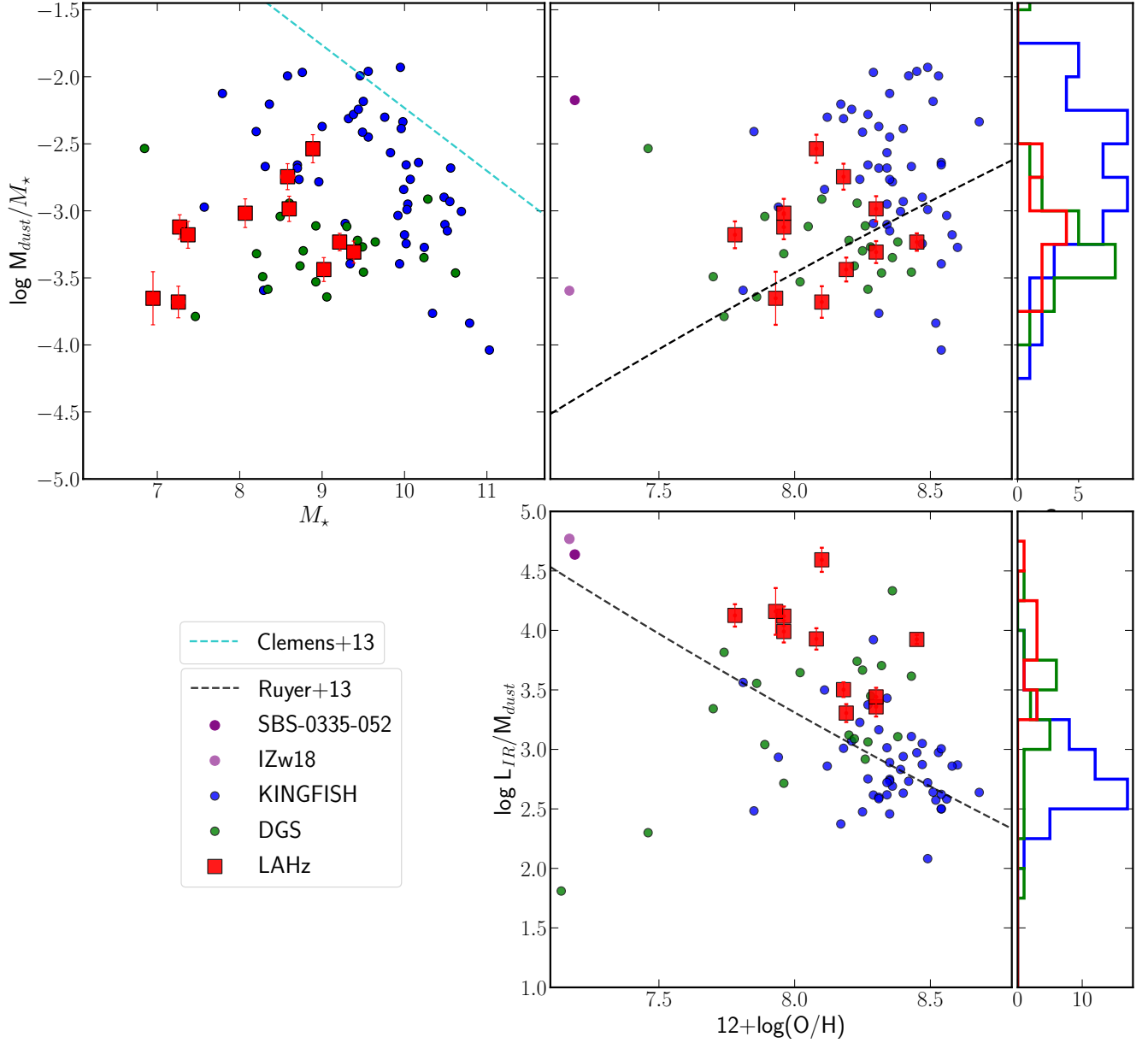


Figure 10. Top left: The dust to stellar mass ratio as a function of stellar mass. The magenta dashed line denotes the relation from Clemens et al. (2013), based on more massive galaxies. **Top right:** Dust to stellar mass ratio as a function of metallicity. The power-law defined by Rémy-Ruyer et al. (2013) is shown as a dashed line. For comparison we include the extremely low-metallicity galaxies SBS-0335 – 052 and IZw18 (purple circles; e.g. Hunt et al. (2014)). **Bottom right:** $L_{\text{IR}}/M_{\text{dust}}$ as a function of metallicity. The dashed line corresponds to the relation found by Rémy-Ruyer et al. (2013). We include SBS-0335 – 052 and IZw18 as purple circles. The histograms on the right show the distribution of each group. In all three panels: red squares are the LAHz candidates; green circles are the DGS sample; blue circles represent the KINGFISH spiral sample.

The high temperatures characterizing the warm dust component of the LAHz galaxies, as well as the high MIR fluxes relative to the peak far-infrared flux of several of the LAHz galaxies, could potentially be due to the presence of a non-stellar heating source, such as an active galactic nuclei (AGN). AGNs in low-mass galaxies are more difficult to detect than their counterparts in massive galaxies. None of our LAHz galaxies are, however, believed to harbor an active AGN. Reines et al. (2020) used the VLA to show that previously identified radio sources that could potentially be AGNs in Haro 02 and Mrk 1307 are most likely associated with star formation activity.

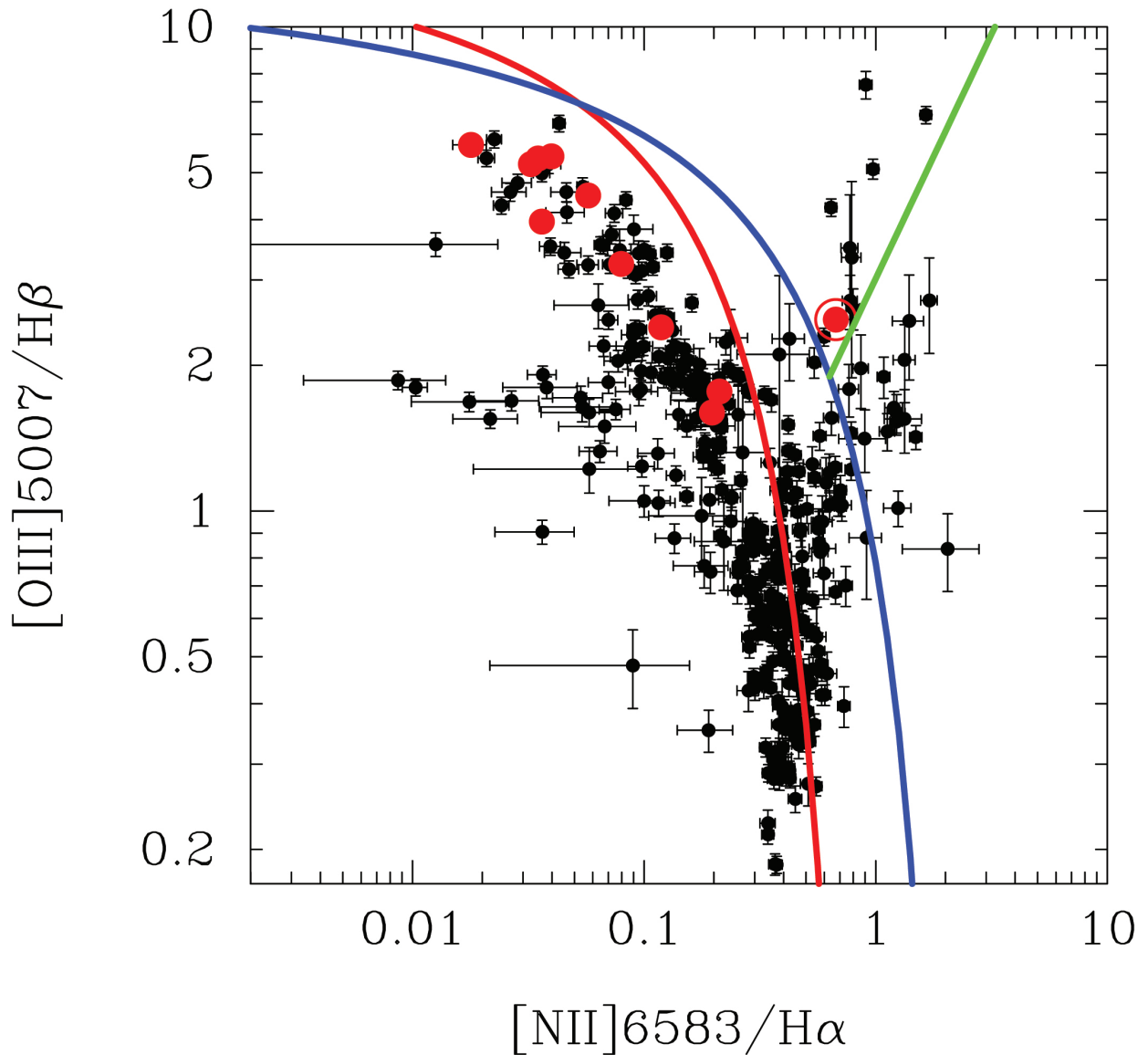


Figure 11. BPT diagram (Baldwin et al. 1981) for nearby galaxies in the Moustakas et al. (2006) sample. This sample contains all eleven of our Local Analog candidates, marked as red circles. The blue line depicts the “maximum starburst line” (Kewley et al. 2001) and is an upper limit for excitation caused by star formation. The red line is an alternate definition based on Sloan Digital Sky Survey galaxies (Kauffmann et al. 2003). The green line divides Seyferts and LINERS (Cid Fernandes et al. 2010).

We explore the possibility of AGN, LINER or Seyfert activity in the LAHz galaxies by plotting them in a BPT diagram (Baldwin et al. 1981). This diagnostic uses the $H\alpha/N[II]$ ratio together with the $[OIII]5007/H\beta$ ratio to distinguish between star formation and AGN activity. The spectral line observations presented in Moustakas et al. (2006) includes all of our LAHz galaxies, and the BPT diagram of the galaxies in Moustakas et al. (2006) is shown in Figure 11, with our LAHz galaxies marked as red circles. All LAHz galaxies, except Mrk 140 falls in the star formation part of the diagram. Mrk 140 falls close to the line depicting maximum star formation activity as defined by Kewley et al. (2001). Since there are no other indication suggesting that Mrk 140 harbors an AGN, we will treat it as a pure star-forming system.

6.4. Star Formation Rates

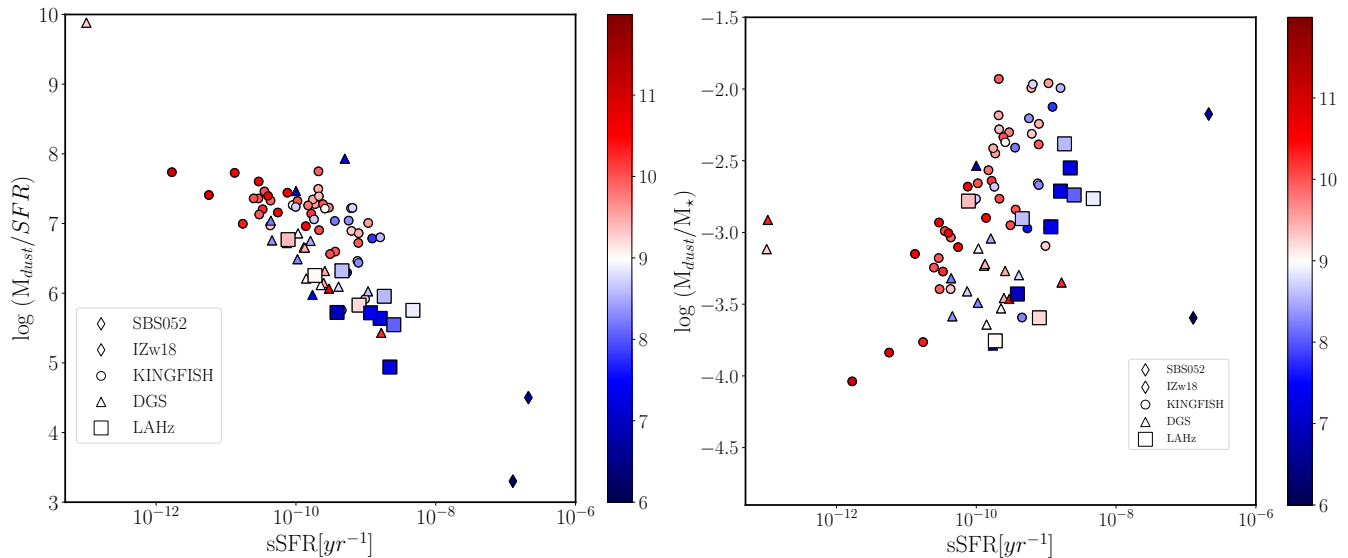


Figure 12. Left: The ratio of dust mass and star formation rate vs specific star formation rate. **Right:** The ratio of dust and stellar mass vs specific star formation rate. In both frames, the LAHz candidates are shown as squares. For reference we include the KINGFISH galaxies as circles (Kennicutt et al. 2011), and the DGS galaxies as triangles (Rémy-Ruyer et al. 2013). The two extreme low metallicity galaxies IZw18 and SBS-0335 – 052 (Hunt et al. 2014) are shown as diamonds. The color indicates stellar mass as shown in the right bar. More massive galaxies are red, less massive are blue.

In Figure 12 we show the correlations between M_{dust}/SFR and $M_{\text{dust}}/M_{\star}$ as a function of the specific star formation rate ($sSFR = SFR/M_{\star}$). As shown in da Cunha et al. (2010), the dust-to-stellar mass ratio strongly correlates with the sSFR, confirming that dust mass and star formation are tightly related. In Figure. 12 we color code the stellar mass of each galaxy. More massive galaxies exhibit a lower sSFR, and higher M_{dust}/SFR ratio, contrary the lower-mass galaxies, which show higher specific SFRs, tracing a clear decreasing relation between $\log(M_{\text{dust}}/SFR)$ and sSFR. In the right panel we plot $M_{\text{dust}}/M_{\star}$ ratio vs. sSFR. Here we see an increasing trend, where $M_{\text{dust}}/M_{\star}$ ratio increases as sSFR increases. Interestingly, the less massive galaxies seem to follow a parallel path to the more massive ones. In both cases, the LAHz candidates fall in the right side, showing that they have higher sSFR than more massive and dusty galaxies.

7. SUMMARY AND CONCLUSIONS

The eleven galaxies designated as potential local analogs of high redshift galaxies (LAHz) were initially selected based on the frequency with which they provide the best fits to the SED of high- z galaxies. They were drawn from the Brown et al. (2014) sample of local galaxy templates, which, although extensive in terms of number of galaxies, only provide a limited set of dwarf irregular galaxies. It is highly likely that there are other local galaxies with similar properties that could fit into the role as LAHz candidates; they just were not part of the Brown sample.

As a group, these eleven LAHz galaxies are similar to galaxies in the more diverse Dwarf Galaxy Survey (Madden et al. 2013). The LAHz galaxies tend to have higher sSFRs, larger $M_{\text{dust}}/M_{\star}$ ratios, and characterized by warmer dust temperatures, than the average for the DGS sample. Despite the small sample size of LAHz candidates, we found that they have different properties. The SFHs for six of the eleven LAHz galaxies are consistent with zero star formation activity at times $\gtrsim 1$ Gyr, making them truly young galaxies. This sub-set of LAHz consists of Mrk 1450, UM 461, Mrk 1307, Mrk 475, UGCA 410, and Mrk 930, and we will refer to it as the ‘gold’ sample. Two of the LAHz galaxies, NGC 2537 and NGC 4670, have SFHs showing significant star formation activity over a Hubble time. These two galaxies, despite their appearance as Blue Compact Dwarf Galaxies, are therefore dominated by an old stellar population, and hence, cannot be representative for high- z galaxies. For the benefit of this discussion, we will refer to these two galaxies as the ‘bronze’ sample. The remaining three LAHz galaxies; Haro 02, Haro 06 and Mrk 140, have

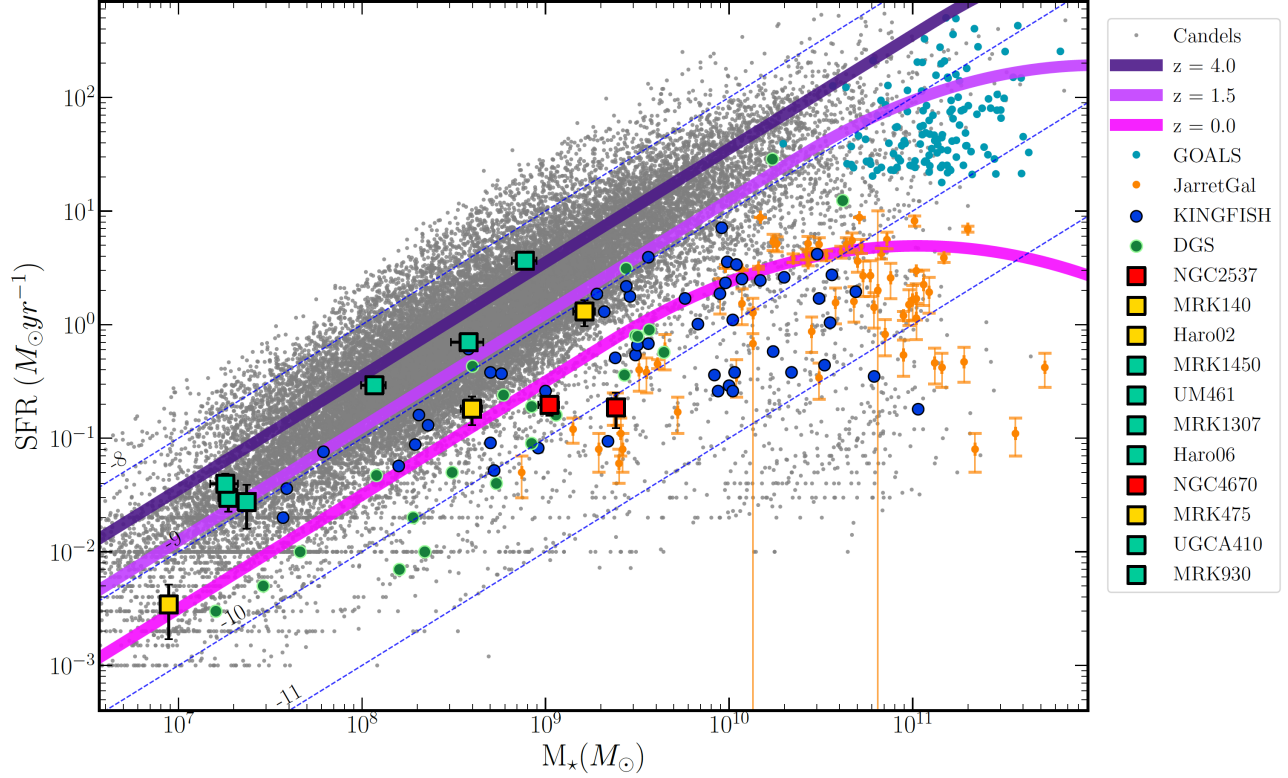


Figure 13. Comparison star formation rate (SFR) vs stellar mass (M_*), the main sequence (MS) is shown in the thick solid line in light-purple for a $z=0$, purple for $z=1.5$, and in dark purple for $z=4$. As a comparison, we show the CANDELS galaxies in gray, the KINGFISH galaxies in orange, the DGS in cyan, the GOALS in green and the Jarrett et al. (2019) Galaxies in light-green. The sample of LAHs (this study), are shown as black squares filled in green whenever they follow the MS for any $z \gtrsim 1.5$, in yellow the MS for any $z \gtrsim 0$ and filled in red when they follow below the MS for $z=0$.

SFHs that cannot rule out star formation activity on longer time scales $\gtrsim 5$ Gyr. Hence, they fall in between the ‘gold’ and ‘bronze’ samples, and we will designate them as the ‘silver’ sample.

While we are dealing with small number statistics, there are several notable differences between the ‘gold’ and ‘bronze’ galaxies; the average sSFR of the ‘gold’ sample is ~ 15 times higher than the average of the two ‘bronze’ galaxies. The average temperature of the cold dust component of the ‘gold’ sample is 48 K, while both the ‘silver’ and ‘bronze’ galaxies have an average T_{cold} of 35 K. These differences could be due to the stochastic nature of star formation activity in these small galaxies. However, it is also accompanied by a systematic difference in gas-phase metallicity; the ‘gold’ sample contains all the most metal-poor systems, $0.19 Z_{\odot}$, while the ‘silver’ and ‘bronze’ samples have an average metallicity of $0.40 Z_{\odot}$. The interstellar gas fractions are 0.68, 0.46 and 0.25 for the ‘gold’, ‘silver’ and ‘bronze’ samples, respectively. Another parameter setting the ‘gold’ galaxies apart is the flux ratio S_{24}/S_{160} , describing the strength of the mid-IR relative to the FIR. These ratios are listed in Table 5. The ‘gold’ sample have an average ratio ~ 0.4 , compared with 0.07 for NGC 2537 and NGC 4670.

In Figure 13 we plot the SFR vs stellar mass for our LAHs galaxies, and several other surveys; including the DGS and KINGFISH samples; the GOALS sample of ultra-luminous infrared galaxies (Armus et al. 2009), and the Jarrett et al. (2019) sample of the 100 largest nearby galaxies. In addition plot high redshift galaxies with $1 < z < 4.5$ from the CANDELS survey (Santini et al. 2015). Diagonal dashed lines show different sSFR values, and the thick diagonal lines show the main sequence for redshifts $z=0$, 1.5 and 4 (Schreiber et al. 2015). Our LAHs galaxies are shown as squares, with colors corresponding to whether they belong in the ‘gold’ (green), ‘silver’ (red), or ‘bronze’ (orange) samples. Most of the DGS, KINGFISH, and Jarrett et al. (2019) galaxies are centered around the main sequence (MS) for $z=0$, including the turn-off at high stellar masses. The GOALS galaxies have, not surprisingly, a higher sSFR. The ‘gold’ LAHs galaxies have high sSFR, and are located above the $z=0$ MS. The two ‘bronze’ LAHs (NGC 2537 and

NGC 4670), are located below the $z=0$ MS, and the three ‘silver’ LAHz are on the $z=0$ MS. Hence, the six LAHz in the ‘gold’ sample can be viewed either as $z=0$ starburst systems, or as MS galaxies at $z \sim 1.5-4$.

Based on these findings, we propose that the six galaxies in the ‘gold’ sample are good candidates for follow-up studies, especially determining their gas dynamics. If they truly are young systems, their age puts their formation epoch at $z \sim 0.08$, or a luminosity distance of only ~ 350 Mpc. This short time scale means that gravitational interaction and merging are not likely to be driving the star formation activity.

ACKNOWLEDGMENTS

Based on observations made with the NASA/DLR Stratospheric Observatory for Infrared Astronomy (SOFIA). SOFIA is jointly operated by the Universities Space Research Association, Inc. (USRA), under NASA contract NNA17BF53C, and the Deutsches SOFIA Institut (DSI) under DLR contract 50 OK 0901 to the University of Stuttgart. Financial support for this work was provided by NASA through award #06-0222 issued by USRA. We extend our thanks to the SOFIA science support team, for all the help in the data acquisition and the data analysis process.

REFERENCES

- Adamo, A., Östlin, G., & Zackrisson, E. 2011, *MNRAS*, 417, 1904.
- Ashby, M. L., Mahajan, S., Smith, H. A., et al. 2013, *VizieR Online Data Catalog*, J/PASP/123/1011
- Armus, L., Mazzarella, J. M., Evans, A. S., et al. 2009, *PASP*, 121, 559. doi:10.1086/600092
- Brown, M. J. I., Moustakas, J., Smith, J.-D. T., et al. 2014, *ApJS*, 212, 18.
- Baldwin, J.A., Phillips, M.M., Terlevich, R. 1981, *PASP*, 93, 5
- Barro, G., Pérez-González, P. G., Cava, A., et al. 2019, *ApJS*, 243, 22.
- Beck, S. C., Hsieh, P.-Y., & Turner, J. 2020, *MNRAS*, 494, 1.
- Bertin, E. & Arnouts, S. 1996, *A&AS*, 117, 393.
- Bian, F., Kewley, L. J., Dopita, M. A., et al. 2016, *ApJ*, 822, 62.
- Casey, C. M. 2012, *MNRAS*, 425, 3094.
- Calzetti, D. 1997, *AJ*, 113, 162.
- Calzetti, D., Armus, L., Bohlin, R.C., Kinney, A.L., Koornneet, J., Storchi-Bergmann, T. 2000, *ApJ* 533, 682
- Campos-Aguilar, A., Moles, M., & Masegosa, J. 1993, *AJ*, 106, 1784.
- Cardamone, C., Schawinski, K., Sarzi, M., et al. 2009, *MNRAS*, 399, 1191. doi:10.1111/j.1365-2966.2009.15383.x
- Cid Fernandes, R., Stasinska, G., Schlickmann, M.S., et al. 2010, *MNRAS*, 403, 1036
- Clemens, M. S., Negrello, M., De Zotti, G., et al. 2013, *MNRAS*, 433, 695. doi:10.1093/mnras/stt760
- da Cunha, E., Charlot, S., & Elbaz, D. 2008, *MNRAS*, 388, 1595.
- da Cunha, E., Eminian, C., Charlot, S., et al. 2010, *MNRAS*, 403, 1894.
- de Vaucouleurs, G., de Vaucouleurs, A., Corwin, H. G., et al. 1991, *Third Reference Catalogue of Bright Galaxies*.
- Dahlen, T., Mobasher, B., Faber, S. M., et al. 2013, *ApJ*, 775, 93.
- Davidge, T. J. 1989, *PASP*, 101, 494.
- Draine, B. T. 2003, *ARA&A*, 41, 241.
- Draine, B. T. 2006, *ApJ*, 636, 1114. doi:10.1086/498130
- Draine, B. T. & Li, A. 2007, *ApJ*, 657, 810.
- Dowell, C. D., Cook, B. T., Harper, D. A., et al. 2010, *Proc. SPIE*, 7735, 77356H.
- Eufrazio, R. T., Lehmer, B. D., Zezas, A., et al. 2017, *ApJ*, 851, 10.
- Eufrazio, R. T. 2017, *Astrophysics Source Code Library*. ascl:1711.009
- Elmegreen, D.M., Elmegreen, B.G., Marcus, M.T., et al. 2009, *ApJ*, 701, 306
- Elmegreen, B.G., Zhang, H.-X.Z., Hunter, D.A. 2012, *ApJ*, 747, 105
- Engelbracht, C. W., Rieke, G. H., Gordon, K. D., et al. 2008, *ApJ*, 678, 804.
- Faisst, A. L., Capak, P. L., Yan, L., et al. 2017, *ApJ*, 847, 21.
- Faisst, A. L., Fudamoto, Y., Oesch, P. A., et al. 2020, *MNRAS*, 498, 4192. doi:10.1093/mnras/staa2545
- Fioc, M. & Rocca-Volmerange, B. 1997, *A&A*, 500, 507
- Fioc, M. & Rocca-Volmerange, B. 1999, *astro-ph/9912179*
- Fudamoto, Y., Oesch, P. A., Schinnerer, E., et al. 2017, *MNRAS*, 472, 483. doi:10.1093/mnras/stx1948
- Fudamoto, Y., Oesch, P. A., Faisst, A., et al. 2020, *A&A*, 643, A4. doi:10.1051/0004-6361/202038163
- Galametz, A., Grazian, A., Fontana, A., et al. 2013, *ApJS*, 206, 10.

- Gordon, K. D., Roman-Duval, J., Bot, C., et al. 2014, *ApJ*, 797, 85. doi:10.1088/0004-637X/797/2/85
- Gordon, M. S., Lopez-Rodriguez, E., Andersson, B.-G., et al. 2018, arXiv:1811.03100
- Grogin, N. A., Kocevski, D. D., Faber, S. M., et al. 2011, *ApJS*, 197, 35.
- Gunn, J. E., Siegmund, W. A., Mannery, E. J., et al. 2006, *AJ*, 131, 2332.
- Harper, D. A., Runyan, M. C., Dowell, C. D., et al. 2018, *Journal of Astronomical Instrumentation*, 7, 1840008-1025.
- Heckman, T. M., Hoopes, C. G., Seibert, M., et al. 2005, *ApJL*, 619, L35. doi:10.1086/425979
- Herschel Science, C. 2013, *VizieR Online Data Catalog*, VI/139
- Hildebrand, R. H. 1983, *QJRAS*, 24, 267
- Hoopes, C. G., Heckman, T. M., Salim, S., et al. 2007, *ApJS*, 173, 441.
- Hunt, L.K., Testi, L., Casasola, V., Garcia-Burillo, S., Combes, F., Nikutta, R., et al. 2014, *A&A*, 561, A49
- Izotov, Y.I., Thuan, T.X., Guseva, N.G. 2005, *ApJ*, 632, 210
- Izotov, Y. I., Guseva, N. G., & Thuan, T. X. 2011, *ApJ*, 728, 161. doi:10.1088/0004-637X/728/2/161
- Jarrett, T. H., Cluver, M. E., Brown, M. J. I. Dale, D. A. Tsai, C. W. Masci, F. 2019, *ApJS*, 245, 25.
- Kaaret, P., Schmitt, J., & Gorski, M. 2011, *ApJ*, 741, 10.
- Kauffmann, G., Heckman, T., White, S.D.M., et al. 2003, *MNRAS*, 341, 33
- Kauffmann, G., Heckman, T. M., White, S. D. M., et al. 2003, *MNRAS*, 341, 54.
- Kauffmann, G., Heckman, T. M., Tremonti, C., et al. 2003, *MNRAS*, 346, 1055.
- Kennicutt, R. C., Calzetti, D., Aniano, G., et al. 2011, *PASP*, 123, 1347.
- Kewley, L.J., Dopita, M.A., Sutherland, R.S., Heisler, C.A., Trevena, J, 2001, *ApJ*, 556, 121
- Kim, K. J., Malhotra, S., Rhoads, J. E., et al. 2021, arXiv:2104.08282
- Kovács, A., Omont, A., Beelen, A., et al. 2010, *ApJ*, 717, 29. doi:10.1088/0004-637X/717/1/29
- Koekemoer, A. M., Faber, S. M., Ferguson, H. C., et al. 2011, *ApJS*, 197, 36.
- Kroupa, P. 2001, *MNRAS*, 322, 231.
- Kunth, D., Maurogordato, S., Vigroux, L. 1988, *A&A*, 204, 10
- Guo, Y., Ferguson, H. C., Giavalisco, M., et al. 2013, *ApJS*, 207, 24.
- Lagos, P., Scott, T. C., Nigoche-Netro, A., et al. 2018, *MNRAS*, 477, 392.
- Le Fèvre, O., Béthermin, M., Faisst, A., et al. 2020, *A&A*, 643, A1. doi:10.1051/0004-6361/201936965
- Madden, S. C., Rémy-Ruyer, A., Galametz, M., et al. 2013, *PASP*, 125, 600. doi:10.1086/671138.
- Meier, D. S., Turner, J. L., Crosthwaite, L. P., et al. 2001, *AJ*, 121, 740.
- Mobasher, B., Dahlen, T., Ferguson, H. C., et al. 2015, *ApJ*, 808, 101.
- Moustakas, J., Kennicutt Jr., R.C. 2006, *ApJS*, 164, 81
- Nayyeri, H., Hemmati, S., Mobasher, B., et al. 2017, *VizieR Online Data Catalog*, J/ApJS/228/7
- Noeske, K.G., Papaderos, P., Cairos, L.M., Fricke, K.J. 2003, *A&A*, 410, 481
- Noll, S., Burgarella, D., Giovannoli, E., et al. 2009, *A&A*, 507, 1793.
- Östlin, G., Hayes, M., Duval, F., et al. 2014, *ApJ*, 797, 11.
- Ott, S. 2010, *Astronomical Data Analysis Software and Systems*, XIX, 434, 139.
- Overzier, R. A., Heckman, T. M., Wang, J., et al. 2011, *ApJL*, 726, L7. doi:10.1088/2041-8205/726/1/L7
- Pantoni, L., Lapi, A., Massardi, M., et al. 2021, *MNRAS*.
- Papaderos, P., Guseva, N. G., Izotov, Y. I., et al. 2008, *A&A*, 491, 113.
- Pardy, S. A., Cannon, J. M., Östlin, G., et al. 2014, *ApJ*, 794, 101. doi:10.1088/0004-637X/794/2/101
- Planck Collaboration, Abergel, A., Ade, P. A. R., et al. 2011, *A&A*, 536, A21. doi:10.1051/0004-6361/201116455
- Reines, A. E., Condon, J. J., Darling, J., et al. 2020, *ApJ*, 888, 36. doi:10.3847/1538-4357/ab4999
- Rémy-Ruyer, A., Madden, S. C., Galliano, F., et al. 2013, *A&A*, 557, A95.
- Rémy-Ruyer, A., Madden, S. C., Galliano, F., et al. 2015, *A&A*, 573, C1.
- Scoville, N. Z. & Kwan, J. 1976, *ApJ*, 206, 718. doi:10.1086/154432
- Sargent, W. L. W., Searle, L. 1970, *ApJ*, 162, L155
- Santini, P., Ferguson, H. C., Fontana, A., et al. 2015, *ApJ*, 801, 97.
- Schreiber, C., Pannella, M., Elbaz, D., et al. 2015, *A&A*, 575, A74. doi:10.1051/0004-6361/201425017
- Sebastian, B. & Bait, O. 2019, *ApJL*, 882, L19.
- Sommovigo, L., Ferrara, A., Pallottini, A., et al. 2020, *MNRAS*, 497, 956.
- Stefanon, M., Yan, H., Mobasher, B., et al. 2017, *ApJS*, 229, 32.
- Thuan, T.X., Izotov, Y.I. 2005, *ApJS*, 161, 240
- Temì, P., Marcum, P. M., Young, E., et al. 2014, *ApJS*, 212, 24. doi:10.1088/0067-0049/212/2/24
- Tremonti, C. A., Heckman, T. M., Kauffmann, G., et al. 2004, *ApJ*, 613, 898.

- Vaillancourt, J. E., Chuss, D. T., Crutcher, R. M., et al. 2007, *Proc. SPIE*, 6678, 66780D.
- van Driel, W., Butcher, Z., Schneider, S., et al. 2016, *A&A*, 595, A118.
- Weingartner, J. C. & Draine, B. T. 2001, *ApJ*, 548, 296. doi:10.1086/318651
- Wu, Y., Charmandaris, V., Hunt, L. K., et al. 2007, *ApJ*, 662, 952.
- Yang, H., Malhotra, S., Gronke, M., et al. 2017, *ApJ*, 844, 171. doi:10.3847/1538-4357/aa7d4d
- Young, E. T., Becklin, E. E., Marcum, P. M., et al. 2012, *ApJL*, 749, L17.